Available online at www.sciencedirect.com
ScienceDirect
Precambrian Research 152 (2007) 170–206
Precambrian Research
www.elsevier.com/locate/precamres

Geochemistry and genesis of the banded iron formations of the Cauê Formation, Quadrilátero Ferrífero, Minas Gerais, Brazil

Carlos A. Spier*, Sonia M.B. de Oliveira, Alcides N. Sial, Francisco J. Rios

Minerações Brasileiras Reunidas—MBR, Av. de Ligação 3580, Nova Lima, 34000-000, Minas Gerais, Brazil

Received 5 August 2004; received in revised form 28 September 2006; accepted 9 October 2006

Abstract

The Cauê Formation of the Paleoproterozoic Minas Supergroup hosts banded iron formations (BIFs), locally called itabirites, deposited in shallow marine passive margin settings. Two major compositional types of itabirite, dolomitic and quartz itabirites, are found in the northwestern part of QF. The former consists of alternating dolomite-rich and hematite-rich bands, whereas the latter is formed with alternating quartz-rich and hematite-rich bands. Accessory minerals are chlorite, sericite, and apatite in both types.

Dolomitic and quartz itabirites have a very simple chemical composition. In the dolomitic itabirite, Fe_2O_3 plus CaO, MgO, and LOI range from 95.8 to 97.8%, while in the quartz itabirite, Fe_2O_3 plus SiO_2 range from 94.4 to 99.6%. Both itabirites are highly oxidized and present $Fe^{3+}/(Fe^{2+} + Fe^{3+})$ ratios higher than 0.98, by far superior than the average ratios of Paleoproterozoic BIFs. Trace element concentrations in itabirites are very low, ranging from <10 to 55 ppm. Dolomite shows negative $\delta^{13}C$ values varying from −2.5 to −0.8‰ versus PDB, while the oxygen isotope data display $\delta^{18}O$ values varying from −12.4 to −8.5‰ versus PDB. The $\delta^{13}C$ values of the dolomitic itabirite are in the same range of those of the overlying stromatolitic dolomites of the Gandarela Formation. C and O isotopes, REE signatures, and Y/Ho ratios suggest a marine origin for the sediments of the Cauê Formation. The HREE enrichment pattern exhibited by the itabirites shows a modern seawater REE signature overprinted by a hydrothermal pattern marked by positive Eu anomalies. Very low contents of Al_2O_3 and TiO_2 and a strong positive correlation between them indicate a minor terrigenous component in the chemically-precipitated marine sediments of the Cauê Formation. Differences in the HREE signatures of itabirites suggest that dolomitic itabirite precipitated in shallower waters receiving sediments from the continent, while quartz itabirite precipitated in deeper waters. Sea-level fluctuations caused by marine transgression–regressions possibly contributed to changes in the composition and varied input of the terrigenous sediments. These changes are expressed by the co-existence of dolomitic, quartz, and amphibolitic itabirites in the Cauê Formation, which represent lateral and vertical facies transitions of dolomitic, cherty, and shaly BIFs, respectively.

Keywords: Banded iron formation; Itabirite; Quadrilátero Ferrífero; Cauê Formation; Águas Claras Mine; Iron ore; Dolomite

1. Introduction

Banded iron formations have long been an object of interest because, apart from being the major source of iron ore, they are particularly important for the understanding of atmospheric evolution, the chemical composition of the oceans, and the appearance of life on Earth.

The Cauê Formation of the Minas Supergroup is known for hosting giant iron ore deposits in the Quadrilátero Ferrífero (QF), in the state of Minas Gerais, located in southern Brazil (Fig. 1). About 16% (170 Mt) of the world's iron ore production in 2003 came from deposits hosted in the Cauê Formation (Tex Report,

* Corresponding author. Tel.: +55 31 3289 3484; fax: +55 31 3289 3514.
E-mail address: carlos.spier@caemi.com.br (C.A. Spier).

0301-9268/$ – see front matter © 2006 Elsevier B.V. All rights reserved.
doi:10.1016/j.precamres.2006.10.003

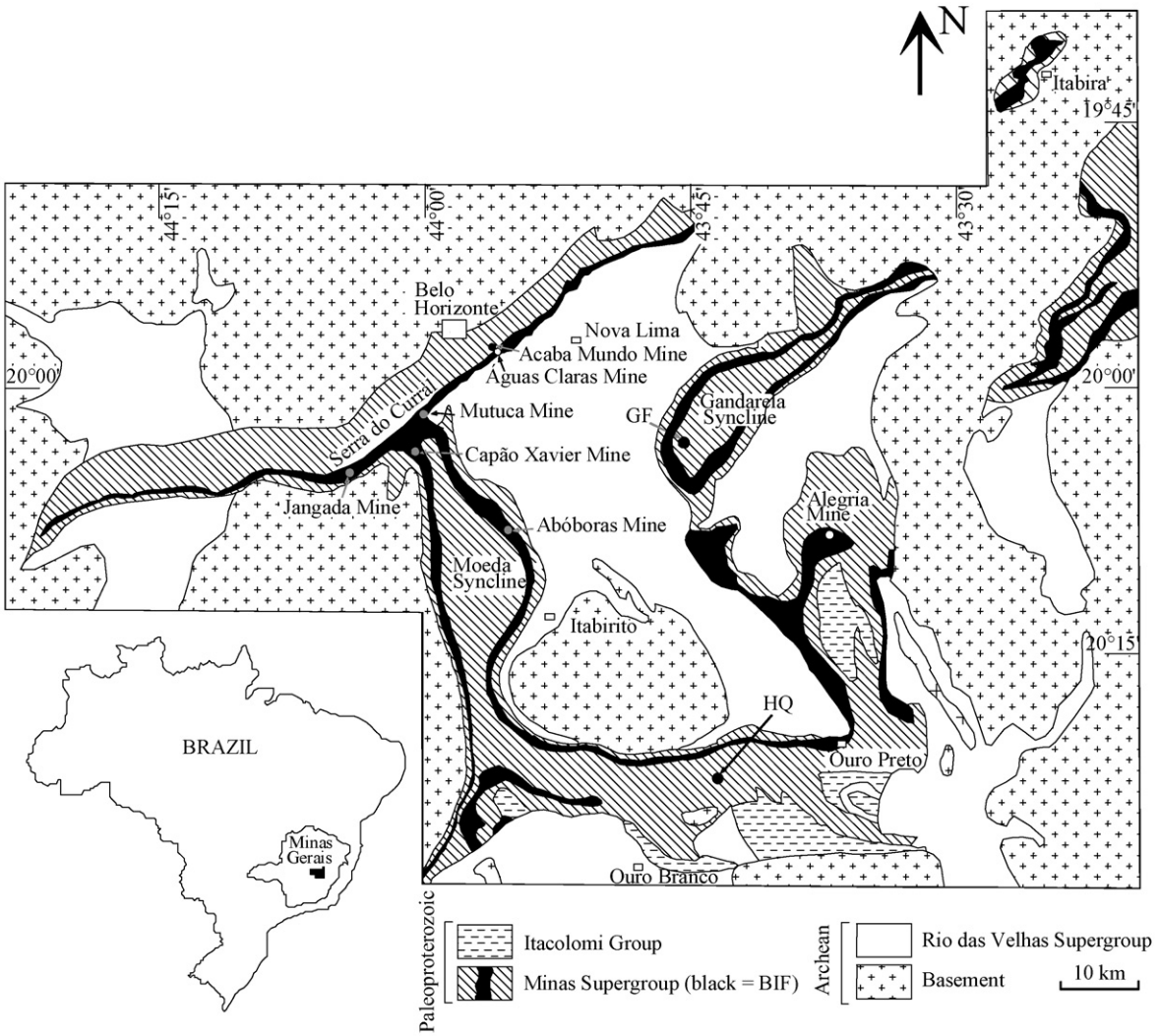

Fig. 1. Location and geological map of the Quadrilátero Ferrífero region (after Dorr, 1969).

2005; Companhia Vale do Rio Doce—CVRD, internal reports). The Cauê Formation is a classical Proterozoic BIF deposited on the continental shelf (Dorr, 1969) and classified a Superior type BIF, according to the scheme of Gross (1980).

Several geological processes have obliterated primary characteristics of the original sediments of the Cauê Formation, resulting in metamorphosed and oxidized BIFs called itabirites in Brazil. Two major compositional types of itabirite occur at the QF: quartzitic, and dolomitic; amphibolitic itabirite is also present, albeit in small amounts (Dorr, 1969; Rosière et al., 1993). The origin of this compositional diversity and the genesis of itabirites are still debated. Can this diversity be accounted for by different original sedimentary facies within the Minas Basin or is it due to post-sedimentary processes? Dorr (1969) correlated the quartz and dolomitic itabirites with the oxide facies BIFs of James (1954) and considered the amphibolitic itabirite a product of contact metamorphism of dolomitic itabirite by adjacent granitic rocks. Beukes et al. (2002) attributed the genesis of the dolomitic itabirite to the hydrothermal metasomatism of the original cherty BIF during a hypogene enrichment stage of the iron ore. Veríssimo (1999) and Veríssimo et al. (2002), however, interpreted compositional variations as representing original sedimentary facies. These authors described the quartz and amphibolitic itabirites at the Alegria Mine, east of the QF (Fig. 1), and corre-

lated them with the oxide and silicate BIFs of James (1954). Literature on the itabirites of the Cauê Formation is very scarce, and most work was conducted during the 1960s and 1970s (e.g., Dorr, 1969, 1973). Recently, Klein and Ladeira (2000) studied the petrology and geochemistry of 16 itabirite samples collected at four different sites of the western QF. Based on minor element and REE geochemistry, they concluded that the itabirites formed by precipitation and deposition from mixed Precambrian seawater and hydrothermal fluids, but provided no detailed explanation for the origin of the dolomitic and quartz itabirite. They also suggested that the observed presence of hematite and absence of magnetite or martite indicate that the hematite was formed by diagenesis or low-grade metamorphism of sedimentary ferric oxides/hydroxides. However, the presence of both martite and relics of magnetite, as well as the formation of hematite after martite, have long been described in itabirites of the QF (Dorr, 1969; Rosière et al., 1993). The genesis of itabirites remains, therefore, subject to debate.

The Águas Claras Mine is located on the northeastern segment of the Serra do Curral Homocline, north of the QF (Fig. 1), where dolomitic and quartz itabirite outcrop. The mining of iron ore over 30 years by Minerações Brasileiras Reunidas (MBR) has exposed a complete unweathered sequence of dolomitic itabirite. In addition, several drill holes intersect fresh quartz itabirite on the northern side of the mine. Unweathered itabirite exposed on mining benches and thousands of meters of drill core allowed the sampling of the entire sequence of the Cauê Formation in this part of the QF. This paper presents the petrological and geochemical data of 48 rock samples collected throughout the Cauê Formation, from its base to the transition zone into the dolomite of the overlying Gandarela Formation. Our aim is to combine petrographic and geochemical analyses in order to evaluate the processes responsible for the formation of the itabirites in the QF.

2. Geological setting

The Cauê Formation and the overlying Gandarela Formation form the Itabira Group, and are the predominant chemical sediments of the Paleoproterozoic Minas Supergroup (Fig. 2). Sediments of the Minas Supergroup were deposited in either an intracratonic basin (Chemale et al., 1994) or in a platform supracrustal setting with a sialic substrate (Cordani et al., 1980; Marshak and Alkmim, 1989; Teixeira and Figueiredo, 1991). They rest unconformably on Archean greenstones of the Rio das Velhas Supergroup and basement granite-gneiss terrains (Chemale et al., 1994).

The Minas Supergroup has clastic sediments of the Caraça Group at the base, which consists of extensive quartzose (Moeda Formation) and argillaceous (Batatal Formation) formations. The Moeda Formation consists of alluvial coarse-grained quartzite, conglomerate, fine-grained marine quartzite, and phyllite (Villaça, 1981). It is conformably overlain by the Batatal Formation, which consists of sericitic phyllite with minor graphitic phyllite. The Caraça Group is interpreted as a transgressive sequence deposited over an old peneplained surface (Villaça, 1981). The Moeda Formation was deposited under paralic to stable shelf environments, while the Batatal Formation comprised offshore sediments deposited on a slowly subsiding continental shelf or platform on a passive margin (Dorr, 1969).

The Itabira Group comprises itabirites (BIFs) with minor dolomite and phyllite of the Cauê Formation and carbonates of the Gandarela Formation; these units are intergradational. Itabirites of the Cauê Formation are lithologically similar to other major oxide facies BIFs (Dorr, 1969). The Gandarela Formation includes dolomites, limestones, dolomitic phyllite, dolomitic iron formation, and phyllite. They were deposited in shallow water and locally have stromatolitic structures (Souza and Müller, 1984). Pb–Pb dating of the stromatolitic dolomite yielded an age of 2420 ± 19 Ma, which is considered by Babinski et al. (1995a) as a depositional age. Based on this upper limit, and considering the Pb–Pb ages on detrital zircons of the Moeda Formation, which vary between 3.0 and 2.6 Ga, Babinski et al. (1995b) suggested that the deposition of the itabirites of the Itabira Group occurred between 2.6 and 2.4 Ga.

The Piracicaba Group at the top of the Minas Supergroup consists of predominantly clastic sediments with minor chemical sediments deposited in marine shallow water and deltaic environments. The Piracicaba Group overlies the Itabira Group, generally with structural conformity, but erosional disconformity has been locally found (Dorr, 1969). Although the tectonic history of the QF remains controversial (e.g., Chemale et al., 1994; Alkmim and Marshak, 1998; Davis and Hippert, 2000), there is a consensus that the rocks of the Minas Supergroup were subjected to at least two main tectonic events during the Proterozoic. Alkmim and Marshak (1998) suggested that the first was Transamazonian (~2.1 Ga) and took place in two stages. The first stage (thrusting stage) occurred shortly after 2.125 Ga and created large northeast-trending anticlines and synclines. It was followed at ca. 2.095 Ga by the second stage (collapse stage), resulting in the development of a dome-and-keel province. The second tectonic event (Brasiliano event, ~0.6 Ga) was compressional and resulted in

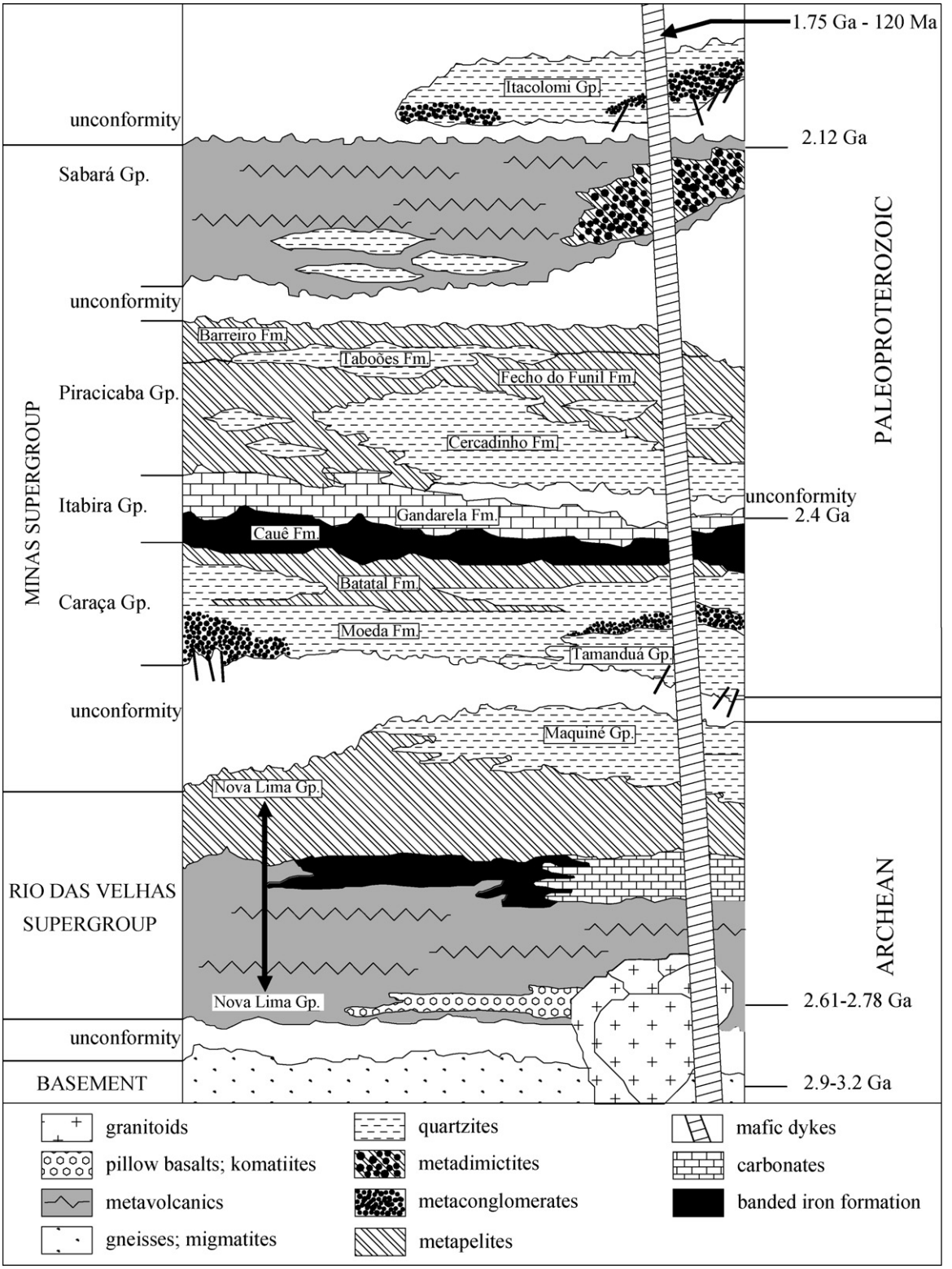

Fig. 2. Stratigraphic column of the Quadrilátero Ferrífero region. The right-hand portion of the column represents relationships in the eastern part of the Quadrilátero Ferrífero, while the left-hand side of the chart represents relationships in the western part of the Quadrilátero Ferrífero (after Alkmim et al., 1998).

a west-verging fold-and-thrust belt causing inversion, amplification, translation, and rotation of basinal synclines, affecting mainly the eastern portion of the QF and obliterating many of the tectonic features of the Transamazonian event (Chemale et al., 1994).

Two main structural domains are recognized at the QF: an eastern, high-strain domain with thick shear zones and major thrust systems, and a western, low-strain domain with well-preserved synclines, discontinuously cut by discrete shear zones and minor thrust faults (Rosière et al., 2001). The metamorphic grade also increases from west to east, from chlorite through biotite and staurolite zones (Herz, 1978). Pires (1995) redefined these metamorphic grade zones as grunerite, cummingtonite, actinolite, and tremolite-anthophyllite zones based on the compositional variation of the amphiboles of the itabirite and phyllite of the Itabira Group. Equilibrium temperatures range from 300 °C on the western side to 600 °C on the eastern side of the QF, with pressures ranging from 3 to 5 kbar, respectively (Pires, 1995).

3. Local geology

The Águas Claras Mine is located at the northern segment of the Serra do Curral, a northeast-southwest trending ∼100 km long ridge that defines the northwest edge of the QF (Fig. 1). The Serra do Curral is a homocline, where bedding dips steeply to the southeast (Pires, 1979; Chemale et al., 1994; Alkmim and Marshak, 1998). Units of the Minas Supergroup crop out along most of its extension as an inverted sequence without repetition. At the northern segment of the Serra do Curral, the rocks are very strained, sinistrally rotated from their original position, and beds are overturned (Chemale et al., 1994). Extensive shear zones occur at the contact between the rocks of the Minas Supergroup and those of the Rio das Velhas Supergroup. In spite of being highly strained, the rocks of the Minas Supergroup were submitted only to green schist facies metamorphism (Pires, 1995).

At the Águas Claras Mine, quartzite and phyllite of the Moeda and Batatal formations, dolomite and itabirite of the Cauê Formation, iron ore and canga (a strongly iron-hydroxide cemented cover) outcrop (Fig. 3A and B). The contact between the stratigraphic units is gradational. Quartzite and phyllite occur at the southern wall of the pit and cap the iron ore body (Fig. 3A). The gradational contact between the Moeda and the Batatal Formations is marked by interfingered lenses of coarse and fine quartzite. Higher in the sequence, fine quartzite lenses are interlayered with sericitic phyllite, which becomes predominant. Lenses of graphitic phyllite with pyrite crystals occur locally, interlayered within the sericitic phyllite.

The contact between clastic sediments of the Batatal Formation and chemical sediments of the Cauê Formation is gradational. It is marked by the appearance of dolomite in the Batatal Formation. Dolomite content increases markedly upwards in the Cauê Formation to form an argillaceous dolomite. Argillaceous dolomite marks the base of the Cauê Formation at the Águas Claras Mine. Lenses of metachert ranging in thickness from tens of centimeters to meters occur within the argillaceous dolomite and grade into quartz itabirite. Fig. 4 shows details of the transition from the Batatal to the Cauê Formation, including the main lithotypes.

The contact between argillaceous dolomite and dolomitic itabirite is characterized by a complex transition zone of approximately 10-m thick, where argillaceous dolomite, ferruginous dolomite, and minor metachert/quartz itabirite occur interlayered. Within this zone, a 80-cm to 2-m thick layer of ferruginous dolomite with peloids, ooids and sub-angular fragments of quartz itabirite cemented by dolomite is observed (Fig. 5A–C). The size of the clasts decreases upsection, suggesting progressive deepening of the basin. This rock is a typical Granular Iron Formation (GIF) in accordance with Trendall's (2002) description. Cracks in individual peloids and in the GIF itself are filled with secondary dolomite. GIF persists laterally for tens of meters along the top of the argillaceous dolomite and grades into quartz itabirite. Transitions between BIFs and GIFs are uncommon in the global stratigraphic record (Beukes and Klein, 1990). They are described only in the transition zone between the microbanded Kuruman Iron Formation, in the granular Griquatown Iron Formation of the Paleoproterozoic sequence of the Transvaal Basin (Beukes, 1980, 1984), and in iron formations of the Frere Formation of the Paleoproterozoic Naberru Basin, Western Australia (Goode et al., 1983).

A ∼6-m thick layer of ferruginous red dolomite within the uppermost part of the transition zone is overlain by dolomitic itabirite. The high content of microcrystalline hematite (see petrography below) is responsible for the red color of the ferruginous dolomite as well as of the dolomitic bands of the dolomitic itabirite.

The appearance of iron mineral bands marks the transition from the ferruginous dolomite to the dolomitic itabirite. This banding corresponds to the mesobanding in the BIFs of the Hamersley Basin defined by Trendall and Blockley (1970). Initially, dolomitic bands are thicker than the iron-rich mesobands. The former range from one to tens of centimeters in thickness,

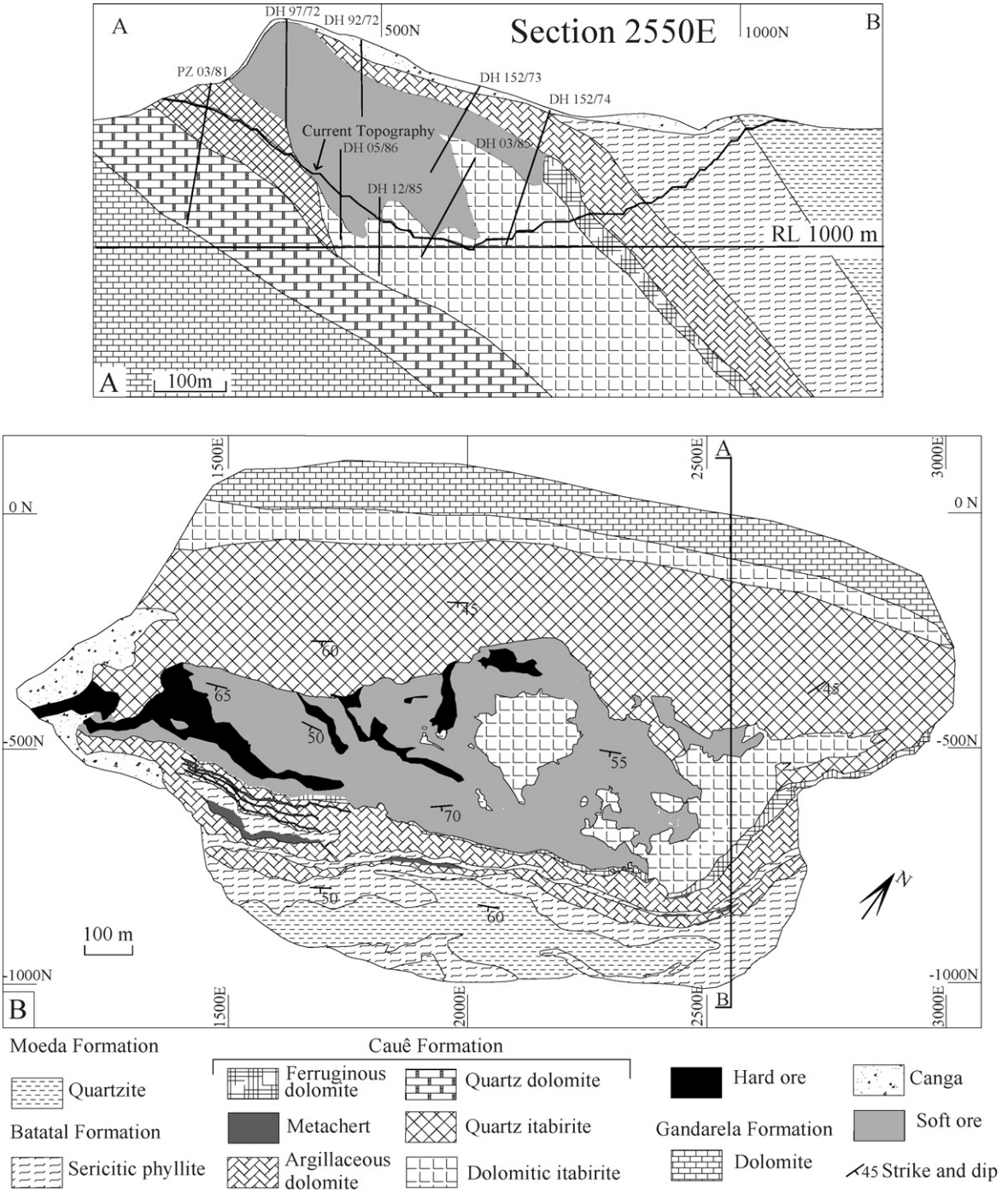

Fig. 3. Águas Claras Mine. (A) Cross section 2550E and (B) geological map.

and vary from deep-red to pink, while iron-rich bands are generally 1–3-cm thick and grey. Locally, both dolomitic and hematitic bands are centimeter-sized in thickness (Fig. 6A). Approximately 50 m from the base of the dolomitic itabirite, dolomitic bands become thinner, forming a more typical dolomitic itabirite. Typical dolomitic itabirite (~250-m thick) exhibits alternating millimeter-thick dolomite and hematite bands (Fig. 6B). Upwards hematitic bands gradually disappear, and dolomitic itabirite grades to a ferruginous dolomite

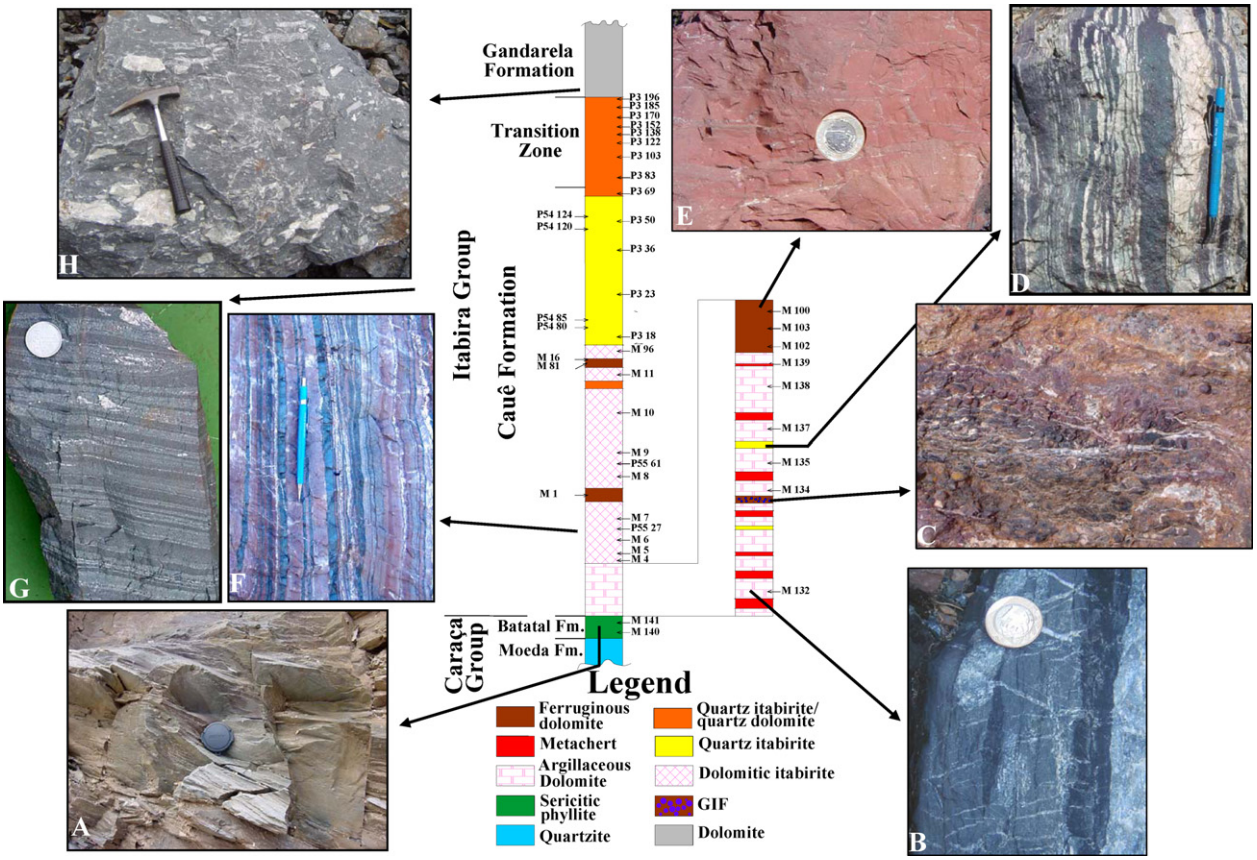

Fig. 4. Detail of the transition zone from the Batatal to Cauê Formation and photographs of the major rock types observed at the profile studied. (A) Sericitic phyllite, (B) argillaceous dolomite, (C) Granular Iron Formation (GIF), (D) quartz itabirite within argillaceous dolomite, (E) ferruginous dolomite, (F) dolomitic itabirite, (G) quartz itabirite, and (H) dolomitic breccia.

which is similar to that present at the base of the Itabira Group.

Within the open pit, dolomitic itabirite is much more common than quartz itabirite, which occurs only on the north wall on the top of the sequence (Fig. 3A). The contact between both rocks is gradational and marked by the appearance of quartz in the dolomitic itabirite and by small lenses of quartz itabirite within the dolomitic itabirite. In drill cores we can see this contact zone containing a triply layered rock with alternating bands of quartz, iron minerals, and dolomite (Fig. 6C). Outside this contact zone, the quartz itabirite exhibits the typical mesobanding of quartz and iron minerals (Fig. 6D). The transition from the quartz itabirite to the carbonate rocks of the Gandarela Formation, observed in drill cores, is also gradational. The gradual appearance of dolomite and the disappearance of hematite and inherent loss of the typical mesoband texture of itabirite characterize the transition zone from quartz itabirite to carbonates. Although dolomitic itabirite and iron ore occur throughout the whole length of the mine along the contact with the Batatal Formation, some exploratory drills completed outside the pit found only quartz itabirite at this equivalent stratigraphic position. This suggests that the transition from dolomitic itabirite to quartz itabirite occurs not only vertically, but also laterally along the Cauê Formation.

The dolomitic itabirite is locally brecciated, with clasts formed either by the hematitic bands or by the dolomitic bands cemented by white carbonate. Some of these breccias suggest a synsedimentary origin; others are typically associated with tension gashes. Several generations of millimetric to centimetric carbonate veins are found crosscutting or parallel to banding. Some of them were affected by the same deformational events that affected the itabirites.

The orebody is a concordant, 2500-m long, roughly tabular-shaped lens that occurs within the dolomitic itabirite, reaching a maximum thickness of 300 m (Fig. 3B). The depth of the ore is variable, extending to over 400 m below the surface and then grading into the proto-ore dolomitic itabirite deeper down (Fig. 3A). The

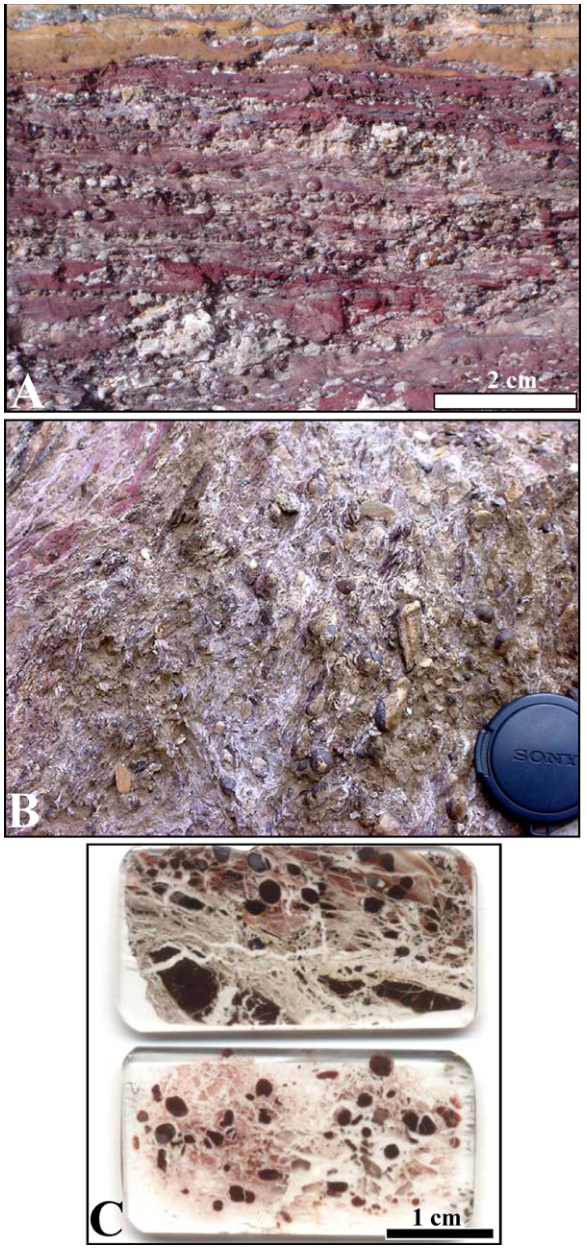

Fig. 5. Photographs of Granular Iron Formation (GIF). (A and B) Outcrop showing ooids and intraclasts cemented by dolomite and sericite/chlorite. (C) Thick section showing ooids and intraclasts cemented by dolomite and sericite/chlorite and cut by secondary dolomite and quartz veins.

iron ore is typically soft (friable) and consists of almost pure hematite, with very low levels of contaminants ($Fe_2O_3 > 98\%$). The soft ore was formed by leaching of the dolomite from the proto-ore rock by supergene fluids and the consequent residual enrichment of the rock (Viel et al., 1987; Spier et al., 2003). For additional information concerning the genesis of this type of ore, refer to Spier et al. (2003), Spier (2005) and Spier et al. (2006).

4. Sampling and analytical procedures

Thirty-four samples of dolomitic and quartz itabirites of the Cauê Formation (Fig. 4) were analyzed for major, traces and rare earth elements (REE). Six samples of dolomitic itabirite had the hematitic and dolomitic bands analyzed separately. Two samples of sericitic phyllite of the Batatal Formation were also analyzed to assess the chemistry of a potentially clastic contaminant of the chemical sediments. Some samples were also analyzed for total graphitic and organic carbon. Sampling was performed mainly at Section 2550E (Fig. 3A), along a ~300-m section of the 1010-m bench, which is located more than 200 m below the current land surface. In this section a representative suite of fresh rocks from the base to the top of the Cauê Formation was collected. Samples of quartz itabirite and dolomite from the transition zone to the Gandarela Formation were collected from drill hole P3 in the same section. Additional samples of dolomitic and quartz itabirite were collected from drill holes P55 and P54 in the proximity to Section 2550E.

To obtain a representative sample, i.e., to overcome the bimodality of the itabirite typical of BIFs everywhere, samples of 3–5 kg (comprising several couplets of mesobands of iron minerals and dolomite/quartz) were selected for bulk analysis. We avoided samples with carbonate or quartz veins to reduce contamination. Six samples of dolomitic itabirite were crushed in a tungsten carbide ringmill and a <0.15-mm fraction of the hematite-rich bands was collected by sieving. The grains were visually inspected under a binocular microscope and handpicked. We also analyzed six samples of visually pure dolomitic bands to accentuate the chemical differences between mesobands.

All samples were ground to a power in a tungsten carbide vessel. Chemical analyses were carried out in Canada at the Activation Laboratories (ACTLABS). Major and trace elements were determined by ICP/ICP-MS after sample fusion with a lithium tetraborate/metaborate. Base metals were determined by ICP-MS/INAA after total digestion by acids. Ferrous iron was determined at the laboratories of MBR by titration with potassium dichromate. The measurements were calibrated against international reference materials, which were analyzed routinely with each sample run. Precision was better than 10% in all cases. The accuracy for major element determinations is estimated to be between 1 and 5%, except for TiO_2 (±20%); and for minor elements, between 5 and 20%, except for deter-

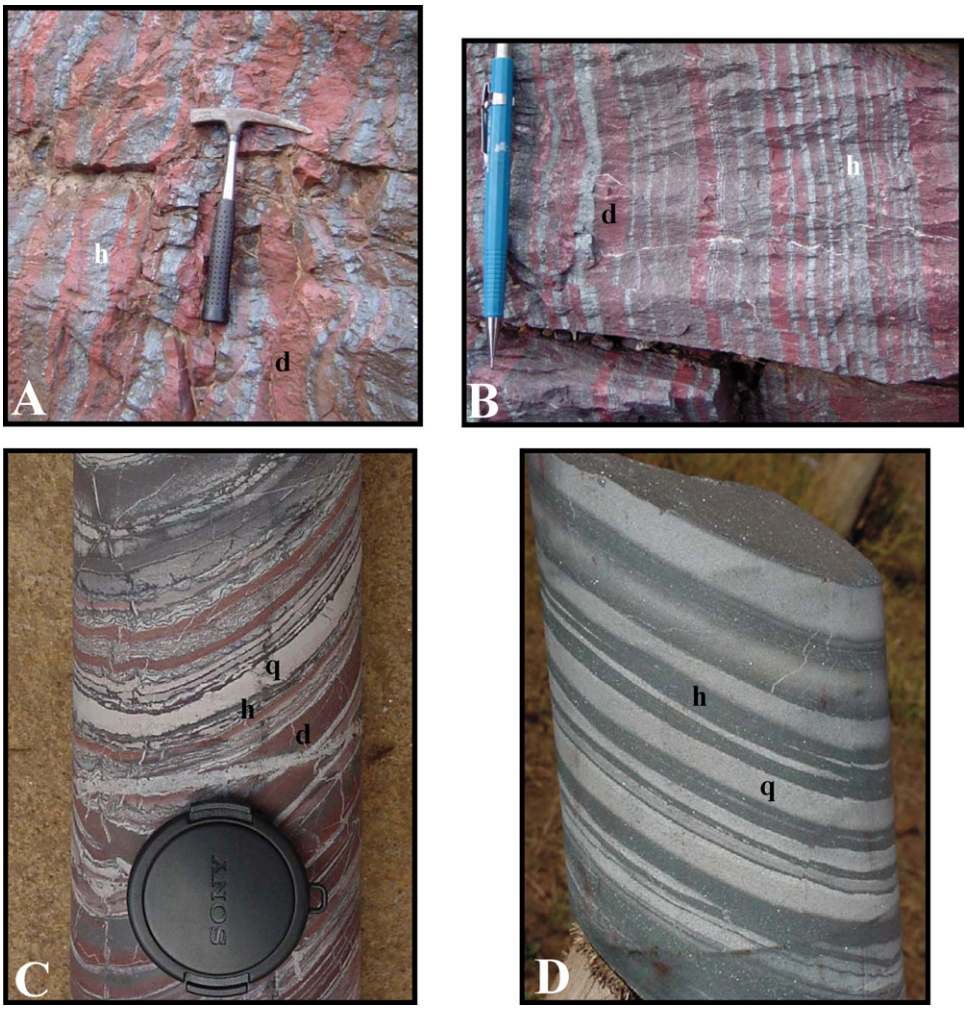

Fig. 6. Photographs of itabirites of the Cauê Formation. (A) Dolomitic itabirite showing thick dolomite mesobands. (B) Typical dolomitic itabirite. (C) Drill core sample of triply layered itabirite showing mesobands of dolomite (d), hematite (h) and quartz (q). (D) Drill core sample of typical quartz itabirite.

minations close to the detection limit, where accuracy is more variable; and for REE, better than 10%.

Forty-two samples of dolomitic bands of dolomitic itabirite were analyzed for carbon and oxygen isotopes. Pure dolomite fragments from thicker mesobands (>1 cm) weighing ~200 g were collected approximately every 10 m from the base to the top of the sequence along the 1010-m bench of the Section 2550E. Isotopic analyses were carried out at the Stable Isotope Laboratory of the Federal University of Pernambuco (NEG-LABISE). CO_2 gas was extracted from powdered carbonates in a high vacuum line after reaction with 100% phosphoric acid at 25 °C for 3 days, and then cryogenically cleaned. The CO_2 gas released was analyzed for O and C isotopes in a double inlet, triple collector SIRA mass spectrometer, using the BSC reference gas (Borborema skarn calcite), that was calibrated against NBS-18, NBS-19, and NBS-20 standards to have $\delta^{18}O$ value of 11.28 ‰ PDB and $\delta^{13}C$ of 8.58 ‰ PDB. The results are expressed in the notation ‰ (per mil) in relation to PeeDee belemnite (PDB). The external precision based on multiple standard measurements of NBS-19 was better than 0.1‰ versus PDB for carbon and oxygen.

Detailed petrographic examination using transmitted and reflected light, scanning electron microscopy (SEM), and electron microprobe analyses (EMP) were carried out to determine the mineralogy and paragenesis of all samples. SEM and EMP analyses were performed at the laboratories of the Geoscience Institute of the University of São Paulo and at the Center for Microscopy and Microanalyses of the University of Queensland, Australia. EMP analyses of dolomite were performed

using a JEOL JXA-8600 electron microprobe operating at 15 kV and 20-ηA current with a focused 5-μm electron beam.

For purposes of chemical data presentation and discussion, the samples analyzed have been divided into five groups on the basis of their chemical compositions and mineral assemblages: (I) sericitic phyllite; (II) argillaceous dolomite; (III) dolomitic itabirite; (IV) quartz itabirite; and (V) quartz-carbonate rocks (transition from the Cauê to the Gandarela Formations). A limit of 2% SiO_2 is set to separate dolomitic from quartz itabirite. We avoided sampling mixed dolomitic and quartz itabirite types to facilitate this separation. A limit of 2% CaO separates quartz itabirite from quartz-carbonate rocks of the transition to the Gandarela Formation.

5. Mineralogy and petrography

5.1. Sericitic phyllite

This unit is a uniform dark-grey, very fine-grained phyllite (Fig. 4A), laminated on a fine scale (1–3-mm thick). Mineralogy consists of quartz and sericite with minor biotite. Texture is lepidoblastic with foliation defined by sericite and biotite. This rock has undergone strong deformation indicated by large porphyroclasts of quartz surrounded by sericite and quartz exhibiting wavy extinction.

5.2. Argillaceous dolomite

The argillaceous dolomite is a black, very fine-grained impure dolomite (Fig. 4B). Local geologists name this rock dolomitic phyllite because, when weathered, it resembles a phyllite. However, the high dolomite content and absence of any well-defined lamination do not allow for the use of the term phyllite. Mineralogically, argillaceous dolomite comprises dolomite (>85%), chlorite, minor quartz, and rare pyrite. Quartz occurs as aggregates showing strong wavy extinction. The absence of hematite and magnetite in argillaceous dolomite distinguishes this rock from the overlying ferruginous dolomite. Argillaceous dolomite is strongly deformed and poorly foliated.

The metachert associated with argillaceous dolomite is a dark, massive, or weakly laminated rock, consisting

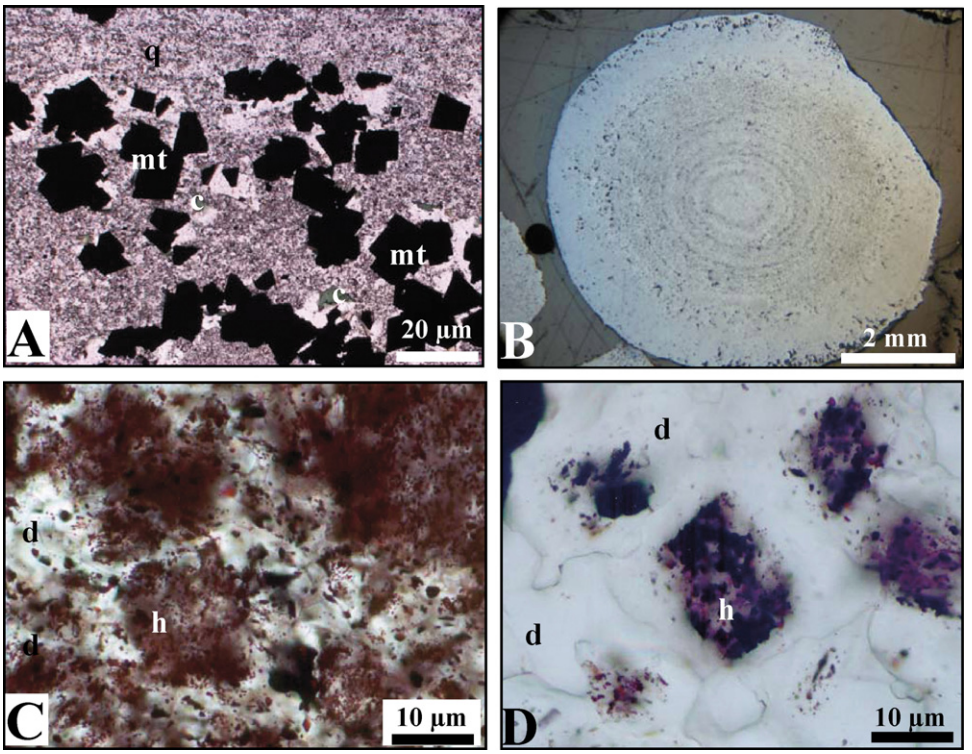

Fig. 7. Photomicrographs of various rock types of the base of the Cauê Formation. (A) Quartz itabirite within argillaceous dolomite; transmitted light (q = quartz). Note the shapes of martitized magnetite (m) and the associated chlorite (c). (B) Ooid within GIF. (C) Inclusions of hematite microcrystals within dolomite crystals forming a dust. (D) Inclusions of hematite microcrystals concentrated within the nuclei of the dolomite crystals which show clean rims.

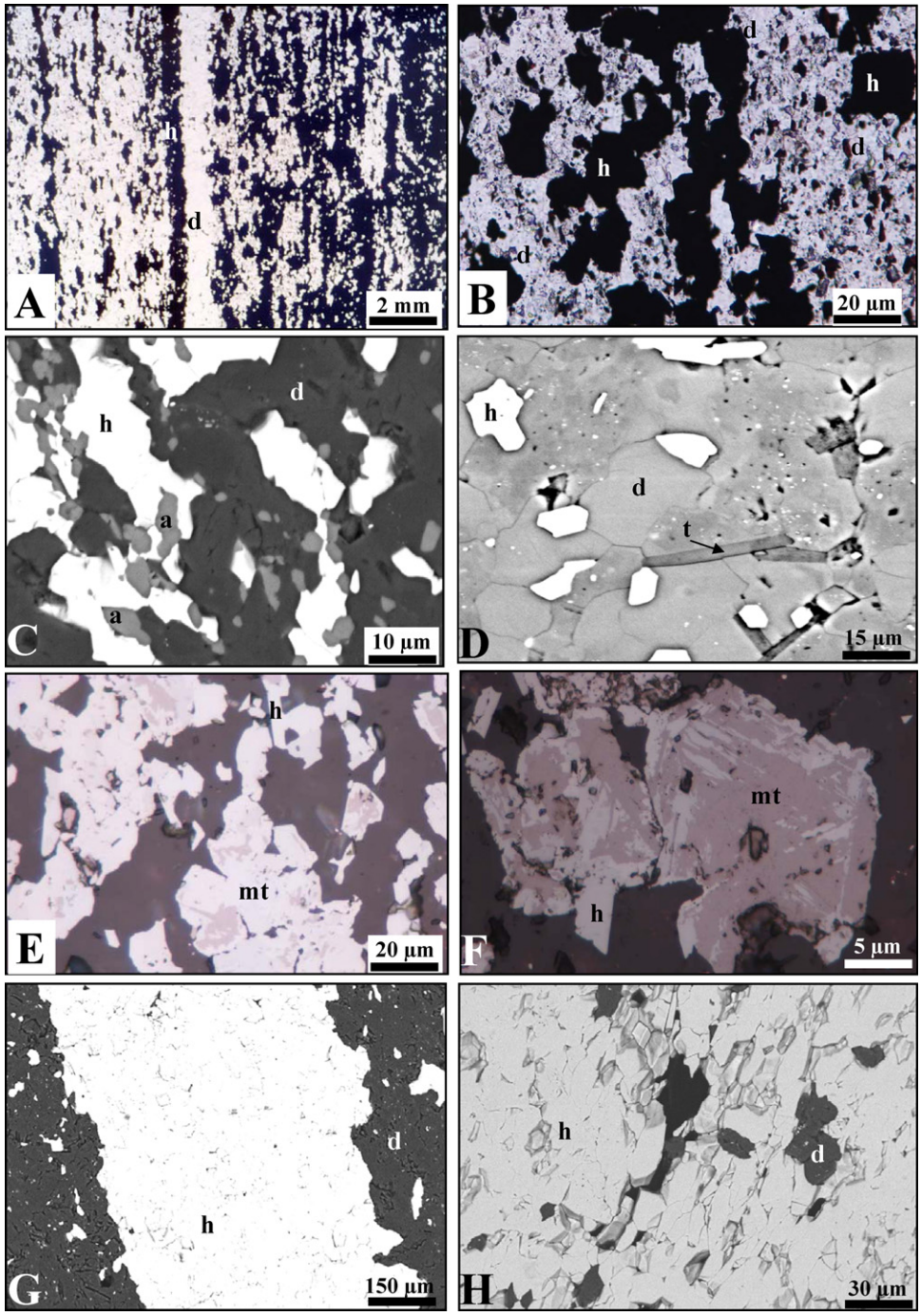

Fig. 8. Photomicrographs and SEM images of the dolomitic itabirite. (A) Microbanding of dolomite-rich and hematite-rich lamina; transmitted light. (B) Detail of the dolomite-rich microband. Euhedral crystals of martite between the dolomite crystals (d); transmitted light. (C and D) Dolomite-rich microband of dolomitic itabirite, SEM images. In (C) dolomite crystals (d) are intergrown with apatite (a) and martite/granular hematite (h). In (D) dolomite crystals (d) are intergrown with talc (t). (E) Relicts of magnetite within martite (mt); reflected light. (F) Detail of a martite crystal showing oxidation of magnetite; reflected light. (G) Hematite-rich microband of dolomitic itabirite, SEM image. (H) Detail of the hematite-rich microbanding showing intergrown martite and granular/tabular hematite (h) with dolomite (d), SEM image.

of microcrystalline quartz with minor dolomite. Towards the top of the sequence, the metachert grades into quartz itabirite which consists of layers of coarse martite with minor quartz and chlorite crystals, alternating with layers mostly composed of microcrystalline quartz with minor amount of dolomite (Fig. 7A).

5.3. Granular Iron Formation

GIF presents granular texture and comprises quartz itabirite and hematite clasts cemented by dolomite (Fig. 5B and C). The clastic fraction contains ooids and angular intraclasts of hematite-rich bands of itabirite. The ooids are rounded, subspherical grains of either itabirite or dolomite, ranging from 0.2 to 5 mm in diameter. Some ooids contain concentric layers of hematite (Fig. 7B). Angular fragments are lithologically similar to itabirite and form tabular fragments up to 2-cm long; smaller ones may be rounded and similar in size to ooids.

5.4. Ferruginous dolomite

The ferruginous dolomite occurs at the base and at the top of the dolomitic itabirite and as meter thick layers randomly distributed within the dolomitic itabirite. Macroscopically and microscopically, ferruginous dolomite resembles the dolomite bands of the dolomitic itabirite, but lacks larger crystals of tabular hematite and martite found in dolomitic itabirite. Ferruginous dolomite is deep red to pink, very fine-grained, and poorly banded (Fig. 4E). It consists of small crystals of dolomite (average grain size of 15 μm) with micrometer size inclusions of dust-like hematite (Fig. 7C). These hematite inclusions are responsible for the strong red color of the rock. They are generally concentrated in the nuclei of dolomite crystals (Fig. 7D). Talc, chlorite, and apatite occur as accessory phases.

5.5. Dolomitic and quartz itabirites

Mesobanding is the most striking macroscopic characteristic of itabirites at the QF and is defined by alternating millimeter- to decimeter-scale hematite-rich bands and dolomite/quartz bands (Fig. 6A–D). Microbanding defined by alternating sub-millimeter hematite and dolomite/quartz lamina are commonly observed within mesobands of itabirites (Figs. 8A and 9A). In dolomitic itabirite, dolomitic bands consist largely of dolomite and up to 40% hematite (Fig. 8B). Talc, chlorite, and apatite occur as accessory minerals (Fig. 8C and D). Thin laminas of apatite parallel to banding are locally observed. Dolomite occurs as euhe-

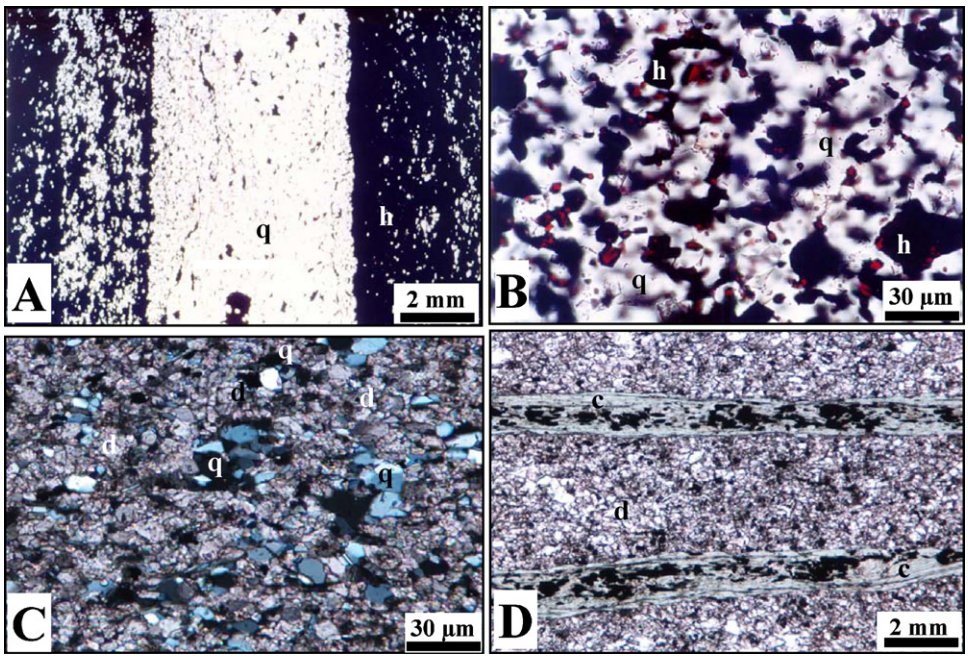

Fig. 9. Photomicrographs and SEM images of quartz itabirite and dolomite of the transition zone to the Gandarela Formation. (A) Microbanding of quartz-rich and hematite-rich lamina; transmitted light. (B) Detail of a quartz-rich lamina of quartz itabirite showing intergrown of quartz (q) and hematite (h); transmitted light. (C and D) Dolomite of the transition zone to the Gandarela Formation, showing in C intergrown dolomite (d), quartz (q), and hematite (h), plane polarized light; in (D) laminaes of chlorite (c) and hematite (black minerals within laminaes), transmitted light.

dral crystals ranging from 2 to 15 μm, intergrown with hematite and accessory minerals (Fig. 8B–D). Micrometer hematite inclusions form an iron dust within dolomite crystals likewise those found in ferruginous dolomite. Hematite in itabirites occurs as aggregates or individual crystals of martite (pseudomorphs of magnetite after oxidation) and tabular hematite; individual crystals vary in size from 5 to 20 μm (Fig. 8E and F). Specularite occurs locally, along shear planes, parallel to or truncating the banding. The hematitic bands are largely comprised of a dense aggregate of hematite crystals, with up to 20% dolomite and traces of talc, chlorite, and apatite (Fig. 8G and H). Thicker hematite bands preserve relict magnetite within martite crystals.

The quartz itabirite is macroscopically and texturally similar to the dolomitic itabirite. The major difference between them is the presence of quartz instead of dolomite (Fig. 9B). Quartz is generally clean, without hematite inclusions, and exhibits wavy extinction. Relics of magnetite are locally observed within martite crystals. When present, dolomite occurs intergrown with quartz (Fig. 9C). Apatite, chlorite, and sericite occur as accessory phases intergrown with quartz and hematite and, locally, as fine inclusions within quartz. The grain size of all minerals is very fine (5–25 μm). Quartz bands of the quartz itabirite consist of quartz with varying proportions of hematite (up to 25%) and accessory minerals (apatite, chlorite, and sericite). Hematite-rich mesobands consist of dense aggregates of hematite with up to 15% quartz.

5.6. Quartz-carbonate rocks of the transition zone to the Gandarela Formation

This group of rocks comprises quartz itabirite-bearing dolomite and dolomite that occurs overlying the quartz itabirite in the transition zone to the Gandarela Formation. The gradual appearance of dolomite and the disappearance of quartz and hematite in quartz itabirite characterize this group. Micro- and mesobanding typical of itabirites are replaced by a poor banding defined by micaceous minerals. The typical dolomite of this zone consists of very fine crystals (average size of 15 μm) with accessory sericite, chlorite, and hematite. Locally, dolomite is enriched with chlorite, which comprises up to 30% of the rock. Chlorite occurs as thin, millimetric laminas, which define conspicuous microbands (Fig. 9D). Talc with minor chlorite and hematite forms thin veins that crosscut chlorite-rich bands.

5.7. Mineral chemistry

Electron microprobe analyses of 26 carbonate samples of argillaceous dolomite, ferruginous dolomite, itabiritic dolomite, and dolomite of the transition zone to the Gandarela Formation indicate that dolomite has approximately equal Ca and Mg concentrations and average CaO and MgO contents ranging from 29.6 to 30.5% and from 18.4 to 20.6%, respectively. FeO and MnO contents are low, ranging from 1.0 to 3.7% FeO and from 0.5 to 0.9% MnO. EMP analyses are summarized in Table 1. The complete dataset is available from the authors upon request as electronic data.

The dolomite composition changes at the transition from argillaceous dolomite to dolomitic itabirite (Fig. 10). Dolomite of argillaceous dolomite has higher FeO and lower MgO contents than dolomite of the overlying rocks. Dolomite of dolomitic itabirite has a very uniform composition throughout the 300-m section. Ca:Mg ratios and FeO plus MnO contents of dolomitic itabirite remain almost constant (around 1:1 and 1.5%, respectively) from the base to the top of the sequence. Dolomite of the transition zone to the Gandarela Formation has higher Ca/Mg ratios and higher contents of FeO and, particularly, of MnO than dolomitic itabirite.

Table 1
Average electron microprobe analyses of dolomite

	Argillaceous dolomite ($n = 28$)	Dolomitic itabirite ($n = 331$)	Dolomite (transition to Gandarela Fm.) ($n = 38$)	Veins ($n = 115$)
wt%				
CaO	29.63	30.51	30.00	30.82
MgO	18.37	20.60	19.00	20.81
FeO	3.66	1.01	2.61	0.74
MnO	0.47	0.60	0.90	0.32
Recalculated on the basis of 2 (Ca, Mg, Fe, Mn)				
Ca	1.003	1.008	1.013	1.016
Mg	0.864	0.947	0.892	0.955
Fe	0.098	0.026	0.069	0.014
Mn	0.013	0.016	0.024	0.014

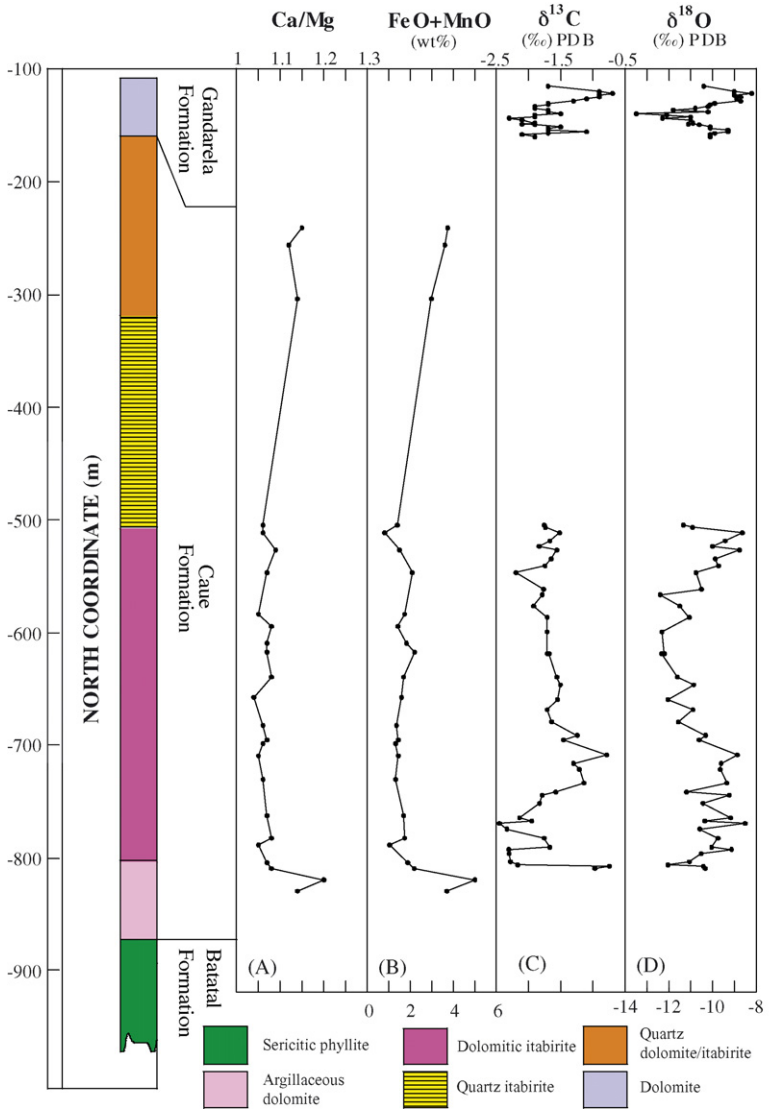

Fig. 10. (A and B) Plots of Ca/Mg ratio and FeO plus MnO contents of dolomite of the dolomitic itabirite as a function of stratigraphic position. (C and D) Plots of $\delta^{13}C$ and $\delta^{18}O$ values of the dolomitic itabirite and stromatolitic dolomites of the Gandarela Formation as a function of stratigraphic position. The data for the Gandarela Formation are from Bekker et al. (2003), obtained from samples collected at the Hargraves Quarry (see Fig. 1 for location).

EMP analyses of carbonate veins that crosscut dolomitic itabirite indicate that dolomite contains on average 30.8% CaO and 20.8% MgO, figures in the range of those for dolomite of host rocks. Contents of FeO and MnO are, however, lower (0.5%). EMP analyses performed on tabular hematite and martite indicate very high and invariant iron contents (>99% Fe_2O_3).

6. Geochemistry

The geochemical data of 36 samples of rocks grouped into five major lithological groups and 12 separate analyses of dolomitic and hematitic bands of dolomitic itabirite are presented in Appendices A and B. Averages of major, trace, and REE are displayed in Tables 2 and 3 according to the lithotype groups. In cases when the results for a few samples were below the detection limit, averages were calculated using half the detection limit for those samples. This procedure was chosen to emphasize samples with values that stood slightly above the detection limit.

Major, trace and REE data for the Post Archean Australian Shale (PAAS) obtained by McLennan (1989) is used for normalization in this paper. The Eu anomaly is

Table 2
Average major and trace element composition

	Sericitic phyllite, $n=2$				Argillaceous dolomite[a], $n=4$				Dolomitic itabirite, $n=11$			
	Avg	Std	Min	Max	Avg	Std	Min	Max	Avg	Std	Min	Max
wt%												
SiO_2	63.33	4.31	60.28	66.38	13.01	4.84	7.37	19.19	1.01	0.46	0.53	1.97
Al_2O	18.61	1.53	17.52	19.69	1.34	0.55	0.61	1.81	0.32	0.25	0.07	0.77
Fe_2O	1.67	0.52	1.31	2.04	1.17	0.92	0.42	2.44	48.90	8.49	39.65	67.61
Fe_{tot}	3.53	2.55	1.73	5.33	5.99	1.83	4.21	8.54	49.64	8.48	40.26	68.11
FeO	1.67	1.82	0.38	2.96	4.34	1.01	3.27	5.49	0.66	0.19	0.44	0.93
MnO	0.03	0.03	<0.01	0.05	0.49	0.16	0.40	0.72	0.28	0.07	0.18	0.43
MgO	3.06	2.60	1.22	4.90	15.59	0.81	14.81	16.72	10.33	1.80	6.49	12.30
CaO	0.11	0.02	0.09	0.12	24.39	1.23	22.63	25.38	14.36	2.42	9.47	17.26
Na_2O	0.07	0.04	0.04	0.09	<0.01				<0.01			
K_2O	5.88	1.20	5.03	6.73	0.30	0.26	0.06	0.59	0.03	0.04	0.01	0.11
TiO_2	0.77	0.03	0.74	0.79	0.06	0.02	0.03	0.08	0.02	0.02	<0.01	0.06
P_2O_5	0.08	0.02	0.06	0.09	0.03	0.01	0.02	0.03	0.12	0.04	0.05	0.19
C_{tot}					10.80	0.61	10.10	11.20	6.45	0.70	5.50	7.05
C_{grap}					0.30	0.06	0.25	0.36	0.03	0.01	0.03	0.05
C_{org}					0.11	0.02	0.10	0.13	0.04	0.01	0.03	0.05
CO_2					38.07	2.25	35.50	39.70	23.60	2.55	20.20	25.80
S	0.008	0.002	0.006	0.009	0.07	0.04	0.03	0.12	<0.001			
LOI	3.99	0.94	3.32	4.65	38.35	1.82	35.67	39.78	22.77	4.15	13.49	27.27
ppm												
Ba	328.0	45.3	296.0	360.0	17.0	8.2	8.0	24.0	12.9	4.3	5.0	19.0
Sr	14.0	4.2	11.0	17.0	21.0	5.1	16.0	28.0	29.8	12.4	17.0	56.0
Y	26.0	1.4	25.0	27.0	8.5	1.7	7.0	11.0	7.7	2.3	4.0	12.0
Sc	16.5	0.7	16.0	17.0	2.3	0.5	2.0	3.0	<1.0			
Zr	178.5	7.8	173.0	184.0	18.3	6.6	11.0	27.0	14.0	5.7	5.0	21.0
Be	2.5	0.7	2.0	3.0	<1.0				<1.0			
V	122.0				13.0	3.2	10.0	17.0	25.6	22.2	5.0	84.3
Ni	66.5	31.0	44.5	88.4	7.9	2.3	5.3	10.2	10.0	8.3	2.8	33.0
Cu	38.2	14.4	28.0	48.3	13.0	5.5	5.7	18.9	7.0	4.0	0.5	10.9
Zn	25.8	25.7	7.6	44.0	<1.0				13.5	12.3	0.5	47.4
Ga	25.5	2.8	23.6	27.5	2.0	0.7	1.0	2.6	<1.0			
Ge	2.7	0.2	2.6	2.9	<0.5				1.8	0.7	<0.5	3.2
Rb	201.1	37.5	174.6	227.6	10.0	7.1	4.4	19.4	<1.0			
Nb	11.1	0.7	10.6	11.6	0.8	0.3	0.4	1.0	0.8	0.5	0.1	1.6
Mo	<2.0				<2.0				<2.0			
Ag	<0.3				<0.3				<0.3			
In	<0.1				<0.1				<0.1			
Sn	3.3	0.4	3.0	3.6	<1.0				<1.0			
Cs	6.8	2.7	4.9	8.7	0.42	0.26	0.14	0.77	<0.1			
$\sum$REE	226.6	8.9	220.3	232.8	34.6	8.3	28.6	46.8	13.9	10.0	7.3	39.8
Hf	5.3	0.1	5.2	5.3	0.5	0.2	0.2	0.8	0.1	0.1	<0.1	0.2
Tl	1.0	0.6	0.6	1.5	0.1	0.1	<0.1	0.3	<0.1			
Pb	14.8	10.7	7.3	22.4	2.3	1.6	1.5	4.8	5.1	3.1	1.5	10.1
Bi	1.5	0.8	1.0	2.1	1.3	0.6	1.0	2.3	1.2	2.2	0.1	6.0
Th	20.4	1.9	19.1	21.7	1.8	0.9	0.7	2.6	0.5	0.4	0.1	1.4
U	5.5	1.6	4.4	6.7	0.8	0.3	0.5	1.2	2.1	1.0	1.0	4.5
As	9.3	9.7	2.5	16.2	<5.0				9.3	9.7	2.5	16.2
Cr	222.1	16.6	210.3	233.8	<20.0				52.9	47.9	<20.0	148.0
Sb	2.8	1.7	1.5	4.0	0.5	0.3	0.3	0.8	1.6	1.0	0.2	3.4
Cd	0.7	0.1	0.6	0.8	1.2	0.8	0.2	2.1	2.0	2.2	0.4	6.2
Fe#	0.57	0.26	0.38	0.76	0.18	0.10	0.07	0.29	0.98	0.01	0.98	0.99

Table 2 (*Continued*)

	Quartz itabirite, $n=9$				Quartz-carbonate rocks, $n=8$			
	Avg	Std	Min	Max	Avg	Std	Min	Max
wt%								
SiO_2	41.74	14.49	19.71	61.95	26.61	17.31	6.56	53.28
Al_2O_3	0.18	0.15	0.06	0.52	0.70	0.98	0.08	3.07
Fe_2O_3	55.71	13.54	37.18	76.75	19.74	12.85	5.20	37.08
Fe_{tot}	56.50	13.95	37.37	79.34	21.70	11.56	8.32	37.40
FeO	0.71	0.79	0.12	2.33	1.77	1.44	0.29	4.32
MnO	<0.01				0.38	0.18	0.09	0.66
MgO	0.14	0.25	0.01	0.80	10.64	6.09	1.79	18.44
CaO	0.46	0.58	0.06	1.69	15.08	8.26	2.98	25.87
Na_2O	<0.01				0.05	0.04	0.01	0.10
K_2O	<0.01				0.03	0.04	0.01	0.10
TiO_2	<0.01				0.05	0.08	0.00	0.26
P_2O_5	0.13	0.09	0.03	0.32	0.06	0.05	0.02	0.17
C_{tot}					7.58	2.54	4.80	9.80
C_{grap}					<0.05			
C_{org}					<0.05			
CO_2					27.78	9.29	17.60	35.90
S	<				<			
LOI	0.59	0.78	<0.02	2.23	23.79	13.05	4.51	39.83
ppm								
Ba	15.4	6.4	5.0	21.0	7.3	3.9	4.0	16.0
Sr	5.0	2.8	1.0	8.0	24.8	12.9	8.0	41.0
Y	3.9	1.4	1.0	6.0	4.6	2.3	3.0	9.0
Sc	<1.0				<1.0			
Zr	12.0	4.6	7.0	20.0	13.4	9.3	4.0	35.0
Be	<1.0				<1.0			
V	22.6	16.2	2.5	52.0	8.9	9.9	2.5	32.4
Ni	10.5	4.6	4.7	20.0	13.6	10.6	2.8	36.8
Cu	<1.0				2.8	3.1	<1.0	9.1
Zn	2.4	1.8	0.5	5.2	7.5	8.1	0.5	21.0
Ga	<1.0				<1.0			
Ge	3.6	1.2	2.4	6.3	1.9	1.7	0.3	5.2
Rb	<1.0				<1.0			
Nb	0.8	0.8	0.3	2.9	0.7	0.5	0.1	1.8
Mo	<2.0				<2.0			
Ag	<0.3				<0.3			
In	<0.1				<0.1			
Sn	<1.0				<0.1			
Cs	<0.1				<0.1			
$\sum$REE	8.2	3.3	4.1	13.9	9.1	3.1	4.7	15.2
Hf	<0.1				0.2	0.1	<0.1	0.5
Tl	<0.1				<0.1			
Pb	<3.0				4.1	4.2	1.5	13.7
Bi	<0.1				<0.1			
Th	0.1	0.1	0.03	0.4	0.6	0.5	<0.1	1.8
U	1.6	0.7	0.9	3.0	1.1	0.5	0.4	2.1
As	9.7	4.3	2.5	15.6	5.8	6.0	<5.0	19.7
Cr	<20.0				<20.0			
Sb	2.8	0.5	1.6	3.3	1.1	0.8	0.3	2.5
Cd	3.0	1.8	0.8	5.5	1.5	1.1	0.4	2.8
Fe#	0.99	0.01	0.97	1.00	0.84	0.17	0.57	0.99

Table 2 (*Continued*)

	Dolomitic itabirite							
	Dolomite-rich band, $n=6$				Iron-rich band, $n=6$			
	Avg	Std	Min	Max	Avg	Std	Min	Max
wt%								
SiO_2	0.73	0.80	0.14	2.31	0.91	0.25	0.62	1.27
Al_2O_3	0.33	0.37	0.07	1.02	0.28	0.13	0.10	0.47
Fe_2O_3	10.93	7.42	4.49	23.92	77.88	8.32	65.04	84.77
Fe_{tot}	11.74	7.46	6.15	25.00	78.23	8.24	65.57	85.13
FeO	0.73	0.45	0.19	1.49	0.32	0.09	0.21	0.48
MnO	0.50	0.10	0.32	0.62	0.12	0.06	0.06	0.20
MgO	18.50	1.51	15.99	19.73	4.11	1.60	2.92	6.51
CaO	26.19	2.09	22.62	28.40	5.45	2.52	3.08	9.18
Na_2O	0.05	0.09	0.01	0.23	<0.01			
K_2O	0.06	0.06	0.01	0.13	0.02	0.02	0.01	0.06
TiO_2	<0.01				<0.01			
P_2O_5	0.06	0.08	0.02	0.22	0.12	0.07	0.04	0.20
S	<0.01				<0.01			
LOI	40.98	3.64	34.51	43.91	9.91	4.25	6.07	16.30
ppm								
Ba	20.7	11.8	7.0	37.0	11.2	2.1	8.0	14.0
Sr	46.2	16.2	29.0	74.0	12.8	3.9	8.0	19.0
Y	9.5	2.6	5.0	13.0	4.7	1.4	3.0	6.0
Sc	<1.0				<1.0			
Zr	8.0	4.6	1.0	15.0	14.7	0.5	14.0	15.0
Be	<1.0				<1.0			
V	10.2	6.4	<5.0	20.2	36.3	42.1	13.0	121.0
Ni	7.3	3.1	2.6	10.9	15.1	5.5	9.8	25.2
Cu	5.2	3.7	1.8	11.6	<1.0			
Zn	7.4	5.2	<1.0	15.0	12.9	1.2	11.6	14.3
Ga	<1.0				0.8	0.5	<1.0	1.5
Ge	<0.5				3.6	0.7	2.6	4.5
Rb	<1.0				1.2	1.3	<1.0	3.8
Nb	0.9	0.3	0.6	1.4	0.4	0.2	<0.2	0.7
Mo	<2.0				1.5	1.2	<2.0	3.9
Ag	<0.3				0.4	0.2	<0.3	0.6
In	<0.1				<0.1			
Sn	<1.0				<1.0			
Cs	<0.1				0.2	0.3	<0.1	0.8
$\sum$REE	18.8	8.4	11.8	33.9	9.6	1.1	8.2	10.8
Hf	<0.1				<0.1			
Tl	<0.1				<0.1			
Pb	7.0	2.4	<3.0	9.4	<3.0			
Bi	<0.1				<0.1			
Th	0.8	0.8	0.2	2.4	0.2	0.1	0.1	0.4
U	1.7	0.6	0.9	2.4	2.1	0.7	1.4	3.0
As	4.8	2.0	<5.0	7.1	6.5	4.2	<5.0	13.8
Cr	23.5	19.4	<20.0	60.0	<20.0			
Sb	1.5	1.7	0.3	4.9	1.3	0.5	0.5	1.8
Cd	0.4	0.2	0.01	0.7	4.6	1.1	2.8	6.0
Fe#	0.91	0.09	0.73	0.97	1.00	0.00	0.99	1.00

Fe_{tot} expressed as Fe_2O_3. $Fe\# = Fe^{3+}/(Fe^{3+} + Fe^{2+})$.

[a] Samples M138 and M139 of metachert were excluded.

Table 3
Average rare earth element composition (ppm)

Litho	Seric. Phyl. ($n=2$)	Arg. Dol.[a] ($n=4$)	Dol. Itabir.[b] ($n=9$)	Quartz Itabir. ($n=9$)	Dolomite (transition to Gandarela Fm) ($n=8$)	Dol. Itabir.	
						Iron-rich band ($n=6$)	Dolomite-rich band ($n=6$)
La	49.09	6.24	2.65	1.40	1.34	1.85	3.13
Ce	101.36	13.34	4.21	2.32	3.02	3.00	6.24
Pr	11.00	1.56	0.53	0.32	0.36	0.39	0.76
Nd	38.42	6.23	2.40	1.59	1.62	1.71	3.41
Sm	7.23	1.47	0.57	0.42	0.41	0.39	0.77
Eu	1.65	0.58	0.22	0.15	0.13	0.14	0.32
Gd	5.46	1.31	0.74	0.54	0.54	0.48	0.99
Tb	0.82	0.24	0.13	0.09	0.10	0.08	0.17
Dy	4.54	1.40	0.86	0.56	0.62	0.54	1.11
Y	26.00	8.50	7.44	4.22	4.75	4.67	9.50
Ho	0.97	0.30	0.20	0.12	0.14	0.13	0.25
Er	2.96	0.96	0.63	0.35	0.42	0.43	0.78
Tm	0.41	0.14	0.10	0.05	0.06	0.07	0.11
Yb	2.63	0.89	0.62	0.30	0.38	0.42	0.71
Lu	0.44	0.14	0.10	0.05	0.06	0.07	0.12
$\sum$REE	226.55	34.61	13.86	8.26	9.20	9.63	18.76
La/Yb_{PAAS}	1.38	0.51	0.27	0.35	0.29	0.32	0.34
La/Nd_{PAAS}	1.15	0.88	0.85	0.88	0.75	0.98	0.82
Ce/Ce^*_{PASS}	1.01	0.99	0.86	0.80	1.01	0.82	0.89
Eu/Eu^*_{PASS}	1.24	1.91	1.60	1.49	1.34	1.57	1.74
Y/Y^*_{PASS}	0.99	1.07	1.63	1.33	1.32	1.40	1.52
Pr/Pr^*_{PASS}	1.04	1.01	1.00	1.00	0.94	1.01	1.00
La/Sm_{PAAS}	1.01	0.62	0.61	0.54	0.51	0.69	0.60
Sm/Yb_{PAAS}	1.39	0.83	0.45	0.70	0.56	0.47	0.58
Sm/Yb	2.74	1.62	0.89	1.38	1.10	0.93	1.15
Y/Ho	26.78	28.83	42.66	36.23	35.00	36.04	38.89

[a] Excluded samples M138 and M139 (metachert).
[b] Excluded samples M4 and M7 (see text for explanation).

defined quantitatively as:

$$\frac{Eu}{Eu^*} = \left(\frac{Eu/Eu_{PASS}}{Sm/Sm_{PASS}} \times \frac{Gd}{Gd_{PASS}}\right)^{1/2}$$

where Eu^* is the hypothetical concentration of Eu. The anomalies of Ce, Pr, and Y were calculated similarly. The degree of light REE enrichment relative to heavy REE is presented as the ratios of PAAS-normalized La and Yb (La/Yb), La and Sm (La/Sm), and Sm and Yb (Sm/Yb).

6.1. Ranges and stratigraphic variation of major elements

The major element composition of the rocks examined is clearly related to their lithotype (Table 2). SiO_2, Al_2O_3, and K_2O are the major constituents of sericitic phyllite with average contents of 63.3, 18.6, and 5.9%, respectively. This rock is also characterized by high TiO_2 (average of 0.8%) and low CaO contents (average of 0.1%).

The argillaceous dolomite exhibits the greatest compositional variation of major elements when compared with other lithotypes (Appendix A); this variation is due to the presence of lenses of the associated metachert and quartz itabirite within the dolomite. CaO (average of 24.4% ranging from 22.6 to 25.4%) and MgO (average of 15.6% ranging from 14.8 to 16.7%) are the main constituents of argillaceous dolomite (not considering samples M138 and M139 of metachert), together with SiO_2, which ranges from 7.4 to 19.2% (average of 13%). Loss on ignition (LOI) is high (average of 38.4%), ranging from 35.7 to 39.8%. This sample group has higher contents of Al_2O_3 than the itabirite and other carbonate-containing groups (average of 1.3%). It is also characterized by the highest concentration of FeO of all sample groups, ranging from 3.3 to 5.5% with an average of 4.3%. The organic carbon content of this group, although very low (average of 0.1%), is the highest of all studied groups.

Bulk analyses indicate that the dolomitic itabirite has high Fe_2O_3 contents, ranging from 39.7 to 67.6% (aver-

age of 48.9%). CaO and MgO contents average 14.4 and 10.3%, respectively. LOI produced by loss of CO_2 from dolomite is highly variable and may be as high as 27% of the total rock weight. Al_2O_3 contents range from <0.1 to 0.8% (average of 0.3%), and Na_2O, K_2O, and TiO_2 contents are very low (average of 0.02%). P_2O_5 contents range from 0.05 to 0.19% and average 0.12%. The $Fe^{3+}/(Fe^{3+}+Fe^{2+})$ ratio for the dolomitic itabirite ranges from 0.98 to 0.99, indicating a very high degree of oxidation.

Chemical analyses of dolomitic and hematitic bands confirm petrographic results, and show that, although dolomite and hematite are dominant in their respective bands, these minerals always co-exist. Thus, dolomitic bands exhibit higher contents of CaO, MgO, and LOI than hematitic bands, but the Fe_2O_3 content reaches up to 24%. Hematitic bands have a Fe_2O_3 content of up to 85%, but CaO and MgO contents reach up 9 and 6%, respectively. The FeO content of dolomitic bands ranges from 0.2 to 1.5% (average of 0.7%); the $Fe^{3+}/(Fe^{3+}+Fe^{2+})$ ratio ranges between 0.73 and 0.97 (average of 0.91). In the hematitic bands, the FeO content ranges from 0.2 to 0.5% (average of 0.3%); $Fe^{3+}/(Fe^{3+}+Fe^{2+})$ ratio ranges from 0.99 to 1.00. Lower $Fe^{3+}/(Fe^{3+}+Fe^{2+})$ ratios observed in the dolomitic bands indicate the presence of Fe^{2+} in the dolomite composition. Otherwise the high $Fe^{3+}/(Fe^{3+}+Fe^{2+})$ ratios in hematitic bands confirms the high degree of oxidation of dolomitic itabirite indicated by the significant martitization of magnetite. Quartz itabirite consists essentially of Fe_2O_3 (average of 55.7%) and SiO_2 (average of 41.7%). CaO, MgO, and LOI are very low, generally below 0.5%. $Fe^{3+}/(Fe^{3+}+Fe^{2+})$ ratios range from 0.97 to 1.00, which is also an indication of the advanced state of oxidation of quartz itabirite.

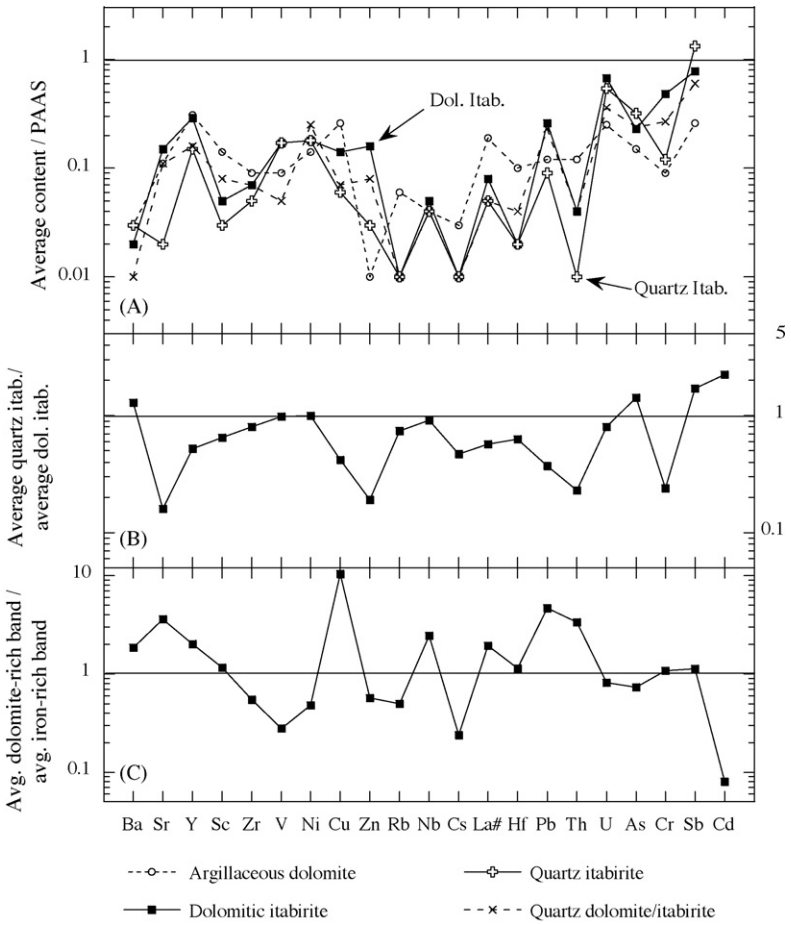

Fig. 11. (A) Average trace element composition of each group of rocks of the Cauê Formation normalized to PAAS. (B) Average trace element composition of quartz itabirite normalized to average composition of dolomitic itabirite. (C) Average trace element composition of dolomite-rich mesoband of dolomitic itabirite normalized to hematite-rich mesoband. La# means $\sum$REE.

6.2. Ranges and stratigraphic variation of trace elements

The concentration of trace elements in all samples is generally very low (<10 ppm). Unlike the major element chemistry that clearly distinguishes each lithotype, trace element concentrations are not as clearly indicative of a particular rock type (Table 2). When compared to the PAAS contents, all lithologies of the Itabira Group are very depleted in trace elements (Fig. 11A).

The argillaceous dolomite from the base of the Cauê Formation and the dolomite from the transition zone to

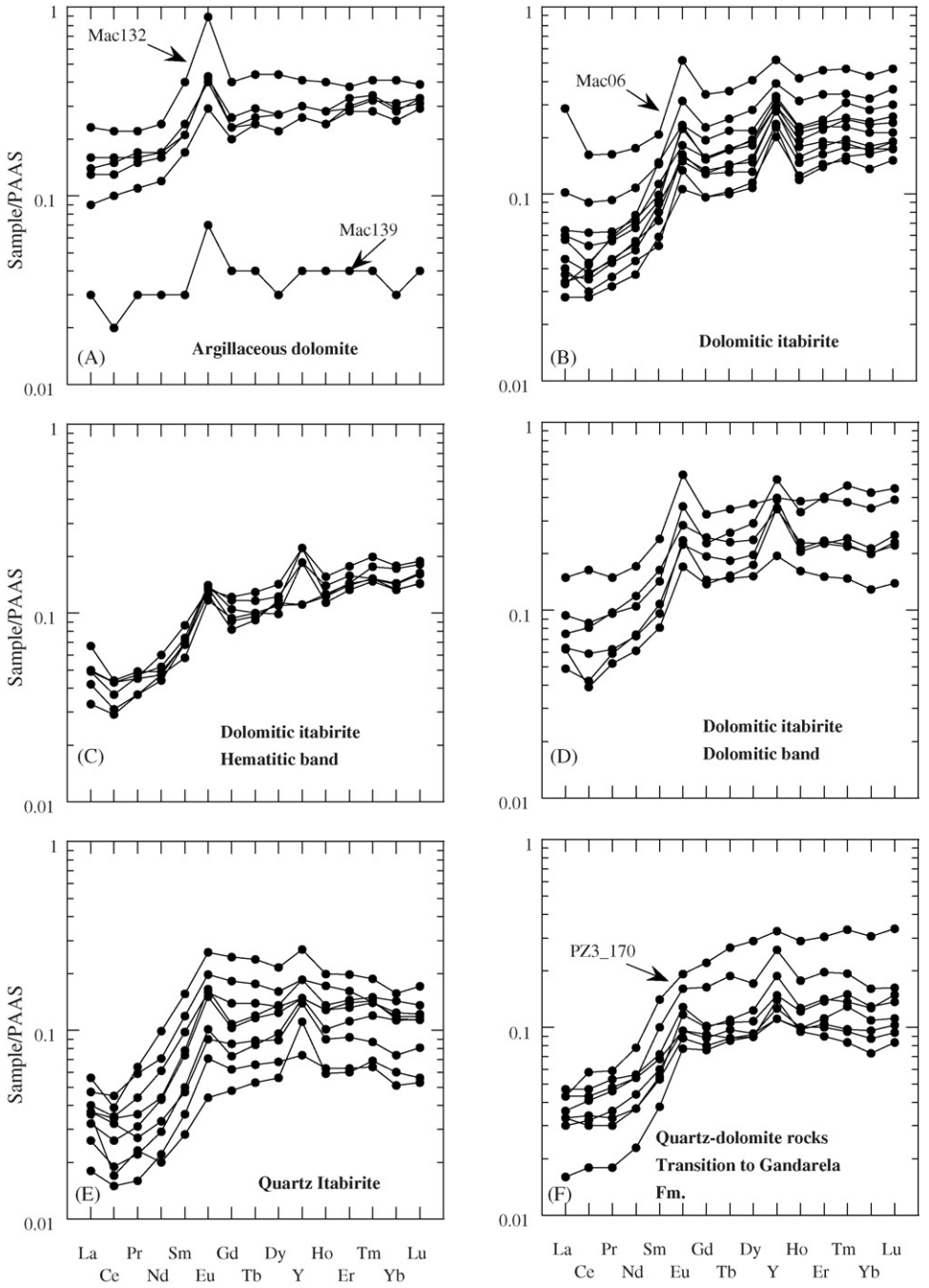

Fig. 12. PAAS-normalized REE data. (A) Argillaceous dolomite. (B–D) Dolomitic itabirite: (B) bulk sample; (C) hematitic band; (D) dolomitic band. (E) Quartz itabirite. (F) Quartz-dolomite rocks of the transition zone to the Gandarela Formation.

the Gandarela Formation have very similar trace element concentrations. The main difference between them are the higher Ba, Cu, Rb, and ∑REE concentrations (average of 17, 13, 10, and 35 ppm, respectively) and lower Zn (<1 ppm, much lower than that of PAAS) of argillaceous dolomite. The quartz and dolomitic itabirites are very depleted in trace elements. Rubidium, Cs, Hf, and Th contents are particularly low in both itabirite types (Table 2). Quartz itabirite is even more depleted in trace elements than dolomitic itabirite (Fig. 11B). The latter is slightly enriched in Sr, Y, Cu, Zn, Pb, Th, and Cr, while the former has higher contents of Sb and Cd. Average trace element concentrations of hematitic bands of dolomitic itabirite normalized to the average concentrations of the dolomitic bands are shown in Fig. 11C. Whereas dolomitic bands have higher Sr (4×), Cu (10×), Pb (5×), and Th (3×) contents, hematitic bands display higher V (4×), Cs (4×), and Cd (13×) contents.

6.3. REE results

REE and Y abundances (REEY) of all samples are listed in Appendix B, and averages of each major lithological group are presented in Table 3. Except for the sericitic phyllite, all lithologies are characterized by low ∑REE, ranging from 8 to 35 ppm. Argillaceous dolomite samples show low ∑REE (average of 35 ppm), but higher than that of overlying itabirites and dolomite. All samples display similar REEY pattern (Fig. 12A) with HREE (La/Yb = 0.51) and MREE (La/Sm = 0.62) enrichments and slight fractionation of HREE (Sm/Yb = 0.83). They show strongly positive Eu anomalies ($Eu/Eu^* = 1.91$), but do not exhibit Ce or Y anomalies, except for sample M139 (metachert), which displays $Ce/Ce^* = 0.90$.

Samples of dolomitic itabirite show an average ∑REE of 14 ppm, ranging between 7 and 40 ppm. REEY patterns of all samples are very similar (Fig. 12B) and show HREE enrichment (La/Yb = 0.27). La/Sm (=0.61) and Sm/Yb (=0.45) ratios for dolomitic itabirite indicate enrichment of heavier REE elements in both the light and heavy REE categories. All samples display strong positive Eu ($Eu/Eu^* = 1.65$) and Y ($Y/Y^* = 1.63$) anomalies and negative Ce anomalies, ranging from 0.74 to 0.97 (Ce/Ce^*).

Dolomite-rich bands of the dolomitic itabirite are more enriched in REE (average ∑REE of 19 ppm) than iron-rich bands (average ∑REE of 10 ppm). The REEY patterns of both bands are similar (Fig. 12C and D) and exhibit the same HREE enrichment of the bulk samples. The major differences between the bands are the more pronounced negative Ce anomaly in iron-rich bands ($Ce/Ce^* = 0.82$) and the less pronounced HREE enrichment in dolomite-rich bands (Sm/Yb = 0.58) when compared to the iron-rich bands (Sm/Yb = 0.47).

Quartz itabirite samples are the most depleted in ∑REE among the whole set of samples studied (average of 8 ppm). Within the LREE they exhibit strong heavy element enrichment (La/Sm = 0.54) similar to that shown by dolomitic itabirite, but with a depletion of the heavy elements within the HREE (Fig. 12E). This is the major distinguishing feature of REEY patterns for both compositional types of itabirites. Positive Eu (average $Eu/Eu^* = 1.49$) and Y ($Y/Y^* = 1.33$) anomalies, and negative Ce anomalies (ranging between 0.60 and 0.93) occur in all samples.

Quartz-carbonate rocks of the transition zone to the Gandarela Formation are likewise the quartz itabirite very depleted in REE (average ∑REE of 9 ppm). All but one sample (P3_170) show similar REEY pattern (Fig. 12F). There is an enrichment of heavier elements within the group of the LREE (La/Sm = 0.51), while HREE have a relatively flat pattern. All samples exhibit positive Eu and Y anomalies, but they are not as pronounced as those of quartz itabirite. There is no Ce anomaly: Ce/Ce^* ranges from 0.93 to 1.16.

6.4. Linear inter-element correlations

Inter-element correlations for samples of dolomitic and quartz itabirites are shown in Table 4. Besides correlations characteristic of each compositional type of itabirite (e.g., strong positive correlations of CaO with MgO ($r \ll 1.0$), LOI ($r \ll 1.0$) and MnO ($r \ll 0.9$), typical of dolomitic itabirite or negative correlations of SiO_2 with CaO ($r \ll -0.9$), characteristic of quartz itabirite), significant correlations are found between Al_2O_3 and TiO_2 ($r \ll 0.9$), Th ($r \ll 0.9$), Zr ($r \ll 0.7$), and ∑REE ($r \ll 0.7$). These correlations are indicative of a terrigenous contribution during the deposition of BIFs (Arora et al., 1995; Beukes and Klein, 1990; Gnaneshwar Rao and Naqvi, 1995; Horstmann and Hälbich, 1995; Manikyamba, 1988).

6.5. C and O isotopes

The 45 analyzed dolomite samples of dolomitic itabirite show negative $\delta^{13}C$ values varying from −2.5 to −0.8‰, and $\delta^{18}O$ values varying from −2.4 to −8.5‰ (Table 5). $\delta^{18}O$ and $\delta^{13}C$ exhibit similar trends along the stratigraphic sequence (Fig. 10C and D). The $\delta^{13}C$ and $\delta^{18}O$ data obtained by Bekker et al. (2003) in stromatolitic dolomites in the upper part of the Gandarela Formation are also shown in Fig. 10C and D.

Table 4
Linear inter-element correlations for all samples of itabirites ($n = 19$)

	SiO_2	Al_2O_3	Fe_{tot}	MnO	MgO	CaO	TiO_2	P_2O_5	LOI	Ba	Sr	Y	Sc	Zr	V
Al_2O_3	−0.26														
Fe_{tot}	−0.08	−0.19													
MnO	−0.87	0.42	−0.31												
MgO	−0.89	0.33	−0.38	0.95											
CaO	−0.90	0.30	−0.37	0.95	1.00										
TiO_2	−0.43	0.90	−0.05	0.55	0.43	0.40									
P_2O_5	0.17	0.01	0.09	−0.12	−0.20	−0.19	−0.09								
LOI	−0.89	0.32	−0.38	0.95	1.00	1.00	0.42	−0.21							
Ba	0.35	−0.27	−0.04	−0.26	−0.31	−0.31	−0.20	−0.20	−0.31						
Sr	−0.76	0.52	−0.35	0.87	0.86	0.85	0.59	0.01	0.85	−0.20					
Y	−0.67	0.56	−0.14	0.75	0.68	0.67	0.64	0.20	0.68	−0.19	0.76				
Sc	−0.26	0.76	−0.19	0.42	0.34	0.30	0.74	0.10	0.32	−0.10	0.62	0.63			
Zr	−0.32	0.70	0.10	0.39	0.26	0.24	0.65	0.02	0.24	−0.15	0.37	0.41	0.42		
V	−0.09	0.37	0.25	0.02	−0.04	−0.04	0.39	−0.17	−0.03	−0.29	−0.09	0.00	−0.01	0.34	
Ni	0.00	0.05	0.26	−0.07	−0.13	−0.13	0.17	−0.24	−0.11	−0.39	−0.30	−0.15	−0.19	−0.07	0.60
Cu	−0.35	0.57	−0.34	0.53	0.48	0.47	0.52	−0.31	0.46	0.02	0.53	0.30	0.36	0.67	−0.07
Zn	−0.50	0.43	0.18	0.44	0.38	0.38	0.61	−0.16	0.39	−0.48	0.34	0.25	0.14	0.32	0.61
Rb	−0.08	0.55	−0.19	0.12	0.17	0.14	0.39	−0.14	0.15	0.06	0.20	0.33	0.58	0.32	−0.04
Nb	0.10	0.45	−0.44	0.13	0.11	0.09	0.35	−0.08	0.10	0.03	0.21	0.16	0.35	0.36	0.20
Cs	−0.17	0.61	−0.22	0.22	0.27	0.24	0.44	−0.08	0.25	−0.05	0.36	0.41	0.71	0.28	−0.08
∑REE	−0.35	0.75	−0.29	0.60	0.46	0.43	0.77	0.24	0.45	−0.08	0.74	0.80	0.84	0.50	0.01
Hf	−0.24	0.67	−0.07	0.34	0.25	0.23	0.84	−0.27	0.25	−0.04	0.35	0.29	0.47	0.40	0.33
Pb	−0.47	0.38	−0.35	0.51	0.61	0.59	0.39	−0.16	0.59	−0.12	0.70	0.28	0.42	0.24	−0.32
Th	−0.47	0.90	−0.24	0.62	0.56	0.52	0.86	−0.03	0.54	−0.19	0.78	0.69	0.87	0.63	0.14
U	−0.15	0.64	−0.09	0.23	0.17	0.16	0.63	0.04	0.18	−0.43	0.13	0.44	0.27	0.33	0.59
As	0.41	0.44	−0.13	−0.20	−0.32	−0.34	0.34	0.19	−0.32	−0.27	−0.10	0.04	0.40	0.00	0.22
Cr	−0.45	0.31	−0.08	0.44	0.46	0.46	0.44	0.07	0.44	−0.10	0.68	0.48	0.33	0.12	−0.14
Sb	0.59	−0.18	0.09	−0.58	−0.60	−0.59	−0.23	−0.04	−0.57	−0.05	−0.68	−0.34	−0.29	−0.42	0.36

	Ni	Cu	Zn	Rb	Nb	Cs	∑REE	Hf	Pb	Th	U	As	Cr
Cu	−0.34												
Zn	0.67	0.15											
Rb	−0.23	0.33	−0.10										
Nb	0.15	0.19	0.19	0.43									
Cs	−0.26	0.33	−0.02	0.96	0.38								
∑REE	−0.23	0.41	0.17	0.30	0.35	0.40							
Hf	0.28	0.43	0.60	0.14	0.23	0.16	0.50						
Pb	−0.32	0.64	0.23	0.28	0.12	0.43	0.32	0.38					
Th	−0.14	0.62	0.38	0.58	0.43	0.70	0.82	0.57	0.61				
U	0.54	0.07	0.57	0.16	0.36	0.14	0.41	0.55	−0.15	0.38			
As	0.37	−0.09	0.14	0.02	0.20	0.08	0.37	0.33	−0.18	0.24	0.54		
Cr	−0.20	0.39	0.36	−0.06	0.01	0.09	0.46	0.39	0.63	0.48	0.09	0.05	
Sb	0.55	−0.60	−0.05	−0.20	−0.05	−0.27	−0.31	−0.07	−0.76	−0.47	0.43	0.57	−0.46

$\delta^{18}O$ values of dolomitic itabirite and those of stromatolitic dolomite are similar and exhibit similar orders of variation. Most samples of the Cauê Formation and Gandarela Formations have $\delta^{18}O$ values above −10.5‰, consistent with those found in well-preserved Paleoproterozoic carbonate successions (Veizer et al., 1989, 1990, 1992; Bekker et al., 2003). ^{13}C contents of dolomitic itabirite are slightly lower than those of dolomite of the Gandarela Formation. The most negative $\delta^{13}C$ values occur at the base of the sequence (−2.4‰), grading up into values around −1.7‰. A red dolomite sampled by Bekker et al. (2003) at the base of the Gandarela Formation (Fig. 1) displayed $\delta^{13}C$ values ranging from −1.3 to −1.0‰. These authors found positive $\delta^{13}C$ values (around +0.4‰) for dolomite at the top of the Gandarela Formation. Carbon isotopic data of the Cauê Formation obtained in this study combined with data for dolomite rocks of the Gandarela

Table 5
C and O isotope composition of dolomite in dolomitic itabirite

Sample	North coordinate (m)	$\delta^{18}O$ (‰) PDB	$\delta^{13}C$ (‰) PDB
MAC-1	−810	−10.33	−0.97
MAC-2	−808	−10.42	−0.75
MAC-3	−807	−12.05	−2.17
MAC-4	−804	−11.06	−2.28
MAC-6	−797	−10.53	−2.30
MAC-8	−793	−9.12	−2.31
MAC-9	−791	−10.05	−1.67
MAC-11	−783	−9.75	−1.76
MAC-12	−775	−10.59	−2.34
MAC-14	−770	−8.50	−2.45
MAC-15	−768	−10.36	−1.95
MAC-16	−765	−9.17	−2.14
MAC-18	−752	−10.44	−1.83
MAC-19	−745	−9.23	−1.79
MAC-20	−742	−11.18	−1.58
MAC-21	−734	−9.34	−1.14
MAC-23	−722	−9.65	−1.21
MAC-24	−717	−9.61	−1.30
MAC-25	−709	−8.86	−0.79
MAC-26	−696	−10.60	−1.46
MAC-27	−692	−10.32	−1.25
MAC-28	−680	−11.57	−1.64
MAC-29	−669	−10.90	−1.71
MAC-30	−660	−12.05	−1.55
MAC-32	−647	−10.85	−1.51
MAC-34	−640	−11.61	−1.56
MAC-36	−629	−12.21	−1.71
MAC-37	−619	−12.34	−1.68
MAC-38	−600	−12.32	−1.71
MAC-39	−587	−11.07	−1.71
MAC-40	−577	−11.49	−1.92
MAC-42	−567	−12.39	−1.79
MAC-43	−562	−10.49	−1.77
MAC-45	−547	−10.74	−2.20
MAC-46	−541	−9.73	−1.75
MAC-47	−535	−9.87	−1.65
MAC-48	−527	−8.76	−1.56
MAC-49	−524	−10.01	−1.84
MAC-50	−519	−9.41	−1.67
MAC-51	−512	−8.63	−1.52
MAC-52	−507	−10.91	−1.74
MAC-53	−505	−11.33	−1.76

Formation suggest a small positive trend (with slight variations) in $\delta^{13}C$ values within the rocks of the Minas Supergroup.

6.6. Comparison with other iron formations

The average major element composition of the dolomitic and quartz itabirite of QF are compared with BIFs of the Carajás Formation (Lindenmayer et al., 2001), the Transvaal Supergroup (Klein and Beukes, 1989) and the Hamersley Group (Taylor et al., 2001) in Table 6. The dolomitic itabirite shows a chemical composition that is very different from that of the other BIFs as a result of its different mineralogical composition. The SiO_2 content of this rock is very low due to the almost complete absence of quartz. However, CaO and MgO contents are the highest of all BIFs studied, reflecting the presence of dolomite. The other major elements are similar to those found in other BIFs. The quartz itabirite shows a very simple major element composition, consisting basically of SiO_2 and Fe_2O_3, with TiO_2, CaO, MgO, MnO, Na_2O, and K_2O contents lower than those of other BIFs. A distinguishing feature of the dolomitic and quartz itabirites of the QF and Carajás, compared to other BIFs, is their higher Fe_2O_3 and lower FeO contents (Table 6). The $Fe^{3+}/(Fe^{3+} + Fe^{2+})$ ratios in BIFs from Transvaal and Hamersley are much lower than 1, while in Brazilian BIFs this ratio is very close to 1 (0.99). This reveals the high degree of oxidation undergone by the BIFs of the QF, since the primary mineral was magnetite, which is regionally recognized as relics in these rocks (Rosière, 1981; Rosière et al., 2001).

The trace element composition of itabirites is similar to that of other BIFs worldwide (Fig. 13A); all contain very low trace element concentrations when compared with PAAS (Fig. 13B). The Ni, Cu, Zn, and Rb contents of the dolomitic and quartz itabirite are lower, and U contents are higher than in other BIFs. The C and O isotopic composition of dolomitic itabirite is distinct when compared to other BIFs considered above (Fig. 14). The $\delta^{13}C$ values of dolomitic itabirite are slightly lower than those of normal marine carbonates, which are typically characterized by $\delta^{13}C$ values of ca. −1‰, but higher than those found in BIFs of the Hamersley and Transvaal Basins. The values of the $\delta^{13}C$ and $\delta^{18}O$ are quite similar to those obtained by Veizer et al. (1990) for dolomites of the Late Archean Wittenoom Formation of the Hamersley Basin, and by Sial et al. (2000) and Bekker et al. (2003) for stromatolitic dolomites of the Gandarela Formation of the Minas Basin.

7. Discussion

7.1. The origin of the dolomitic itabirite

The rocks of the Cauê Formation were subjected to at least two tectonic events – intrusion of granitic and mafic rocks, and metamorphism to green schist facies – that transformed the original BIFs into the itabirites observed today. Recently, proposed genetic models to explain the origin of the high-grade iron ores formed from BIFs involve early hydrothermal silica dissolution

Table 6
Averages of major chemical components (wt%) in bulk analyses of BIFs of the Quadrilátero Ferrífero, Carajás, Hamersley, and Transvaal Basins

	Quadrilátero Ferrífero		Carajás	Hamersley	Transvaal	
	Dolomitic itabirite, $n=11$	Quartz itabirite, $n=9$	Serra Norte[a], $n=30$	Dales Gorge[b], $n=12$	Kuruman oxide BIF[c], $n=9$	Kuruman siderite BIF[c], $n=16$
SiO_2	1.01	41.74	40.60	44.22	46.47	39.99
Al_2O_3	0.32	0.18	0.20	0.38	0.07	0.10
Fe_2O_3	48.90	55.71	56.76	33.27	22.72	1.27
FeO	0.66	0.71	1.07	13.61	17.56	23.86
Total Fe	49.64	56.50	57.95	48.43	42.25	27.80
MnO	0.28	<0.01	0.05	<0.1	0.09	0.32
MgO	10.33	0.14	<0.10	1.83	2.36	5.03
CaO	14.36	0.46	<0.05	1.56	2.89	5.39
Na_2O	<0.01	<0.01	0.04	<0.05	0.02	0.02
K_2O	0.03	<0.01	<0.01	<0.05	0.03	0.02
TiO_2	0.02	<0.01	<0.05	0.007	<0.04	0.04
P_2O_5	0.12	0.13	<0.05	0.20	0.11	0.06
LOI	22.77	0.59	1.28	3.16	7.42	23.89
Fe#	0.99	0.99	0.98	0.69	0.54	0.05

Total Fe reported as Fe_2O_3. Fe# = $Fe^{3+}/(Fe^{3+} + Fe^{2+})$.
[a] Lindenmayer et al. (2001).
[b] Taylor et al. (2001).
[c] Klein and Beukes (1989).

and simultaneous introduction of Ca-Fe-Mg-carbonates in the original iron formation. This would be followed by supergene leaching of carbonates, long after they formed, to create high-grade hematite ores (Taylor et al., 2001; Dalstra and Guedes, 2004; Thorne et al., 2004). Beukes et al. (2002) suggest that the soft high-grade iron ore of the Águas Claras Mine is a supergene-modified hydrothermal ore, considering that the dolomitic itabirite (proto-ore) "*obviously developed from the replacement of chert-bands in iron-formation by carbonate*".

We do not agree with this hypothesis because there is no field evidence to support it. On the contrary, the co-existence of quartz and dolomitic itabirite is locally observed in drill cores and outcrops of the Águas Claras Mine, occasionally forming a triply banded rock (Fig. 6C). Quartz and dolomite are commonly intergrown in metachert, dolomite, and itabirite, without any evidence of metamorphic reaction or hydrothermal substitution. Dolomitic itabirite and dolomite of the Cauê Formation occur throughout the Serra do Curral, outcropping along ca. 80 km, and also being recorded in deep mine exposures and drill cores of the Mutuca, Capão Xavier, and Jangada mines (Fig. 1). Still, there is no direct evidence observed so far of a regional hydrothermal process of dolomitization of the quartz itabirite.

Exposures of dolomitic itabirite interlayered with dolomite and sedimentary dolomitic breccia of the Gandarela Formation are recorded along the benches of the Acaba Mundo Mine, on the north of the Águas Claras Mine (Fig. 1). Interlayering of dolomitic itabirite and dolomite of the Gandarela Formation has long been described at the QF (e.g., Pomerene, 1964; Wallace, 1965; Dorr, 1969) and was also observed in exploratory drill holes conducted by MBR in the Abóboras and Gandarela region (Fig. 1) (MBR, internal reports). This interlayering strongly suggests a sedimentary origin of dolomitic itabirite, since the dolomite of the Gandarela Formation clearly has a sedimentary origin, as indicated by the presence of stromatolites. Accordingly, the dolomitic itabirite would rather represent a facies variation of the BIFs of the Cauê Formation than a product of hydrothermal metasomatism of an original chert BIF.

A marine origin for the dolomitic itabirite is also supported by the C and O isotopes, which are similar to those of other stromatolitic carbonates, e.g., in the Gandarela Formation of the Minas Basin, in the Gamohaan Formation which underlies BIFs of the Kuruman Iron Formation of the Transvaal Basin, and in the Late Archean Wittenoom Formation of the Hamersley Basin (Fig. 14). Carbon isotope data of the Cauê Formation are also similar to those found in marine carbonates older than ca. 2.32 Ga, supporting the interpretation that they are seawater precipitates slightly modified by diagenetic and metamorphic alteration.

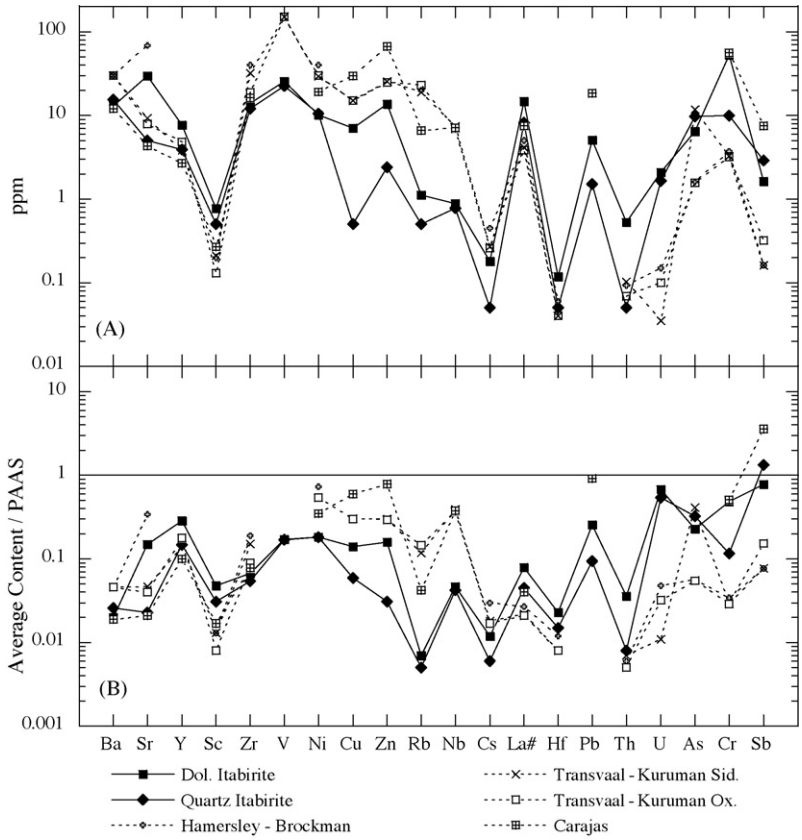

Fig. 13. Average trace element (A) composition of BIFs of Quadrilátero Ferrífero, Hamersley, Transvaal, and Carajás. (B) Trace element composition normalized against PAAS of McLennan (1989), with the exception of Ta, Sb, and As contents that were normalized against NASC of Gromet et al. (1984). The data for Hamersley and Transvaal are from Klein and Beukes (1992). The data for Carajás are from Lindenmayer et al. (2001), with the exception of Pb, Zn, Cu, Sc, and Sb contents, which are from Macambira and Schrank (2002).

Y/Ho ratios of the dolomitic itabirite provide further constraints on its origin. Modern seawater has a Y/Ho ratio (>44) that is substantially higher than chondritic ratios (26–28). The vast majority of geologic materials, including all volcanic rocks and clastic sediments, have chondritic ratios (Nozaki et al., 1997). However, sampled dolomitic itabirites have Y/Ho ratios ranging from 34 to 52, with an average of 42 (Table 3), pointing to the influence of seawater in the precipitation of the carbonate.

The problem with a strictly sedimentary origin of the dolomitic itabirite is that it is nearly impossible to precipitate dolomite, at earth surface temperatures, without bacterial mediation (Warren, 2000). Dolomite, however, is a common mineral component of BIFs, particularly those deposited in shallow waters, where it is usually associated with ankerite and calcite (e.g., Arora et al., 1995; Dymek and Klein, 1988; Ewers and Morris, 1981; Floran and Papike, 1978; Klein and Beukes, 1989), as in the Sokoman Iron Formation in the western edge of the Labrador Trough (Klein and Fink, 1976) and in the Nabberu Basin, Western Australia (Hall and Goode, 1978).

It view of the above arguments, it seems likely that dolomite in the dolomitic rocks of the Cauê and Gandarela Formations is either a carbonate precipitated from seawater through bacterial mediation, or a product of dolomitization of earlier carbonates, a common process in the Proterozoic.

7.2. The composition of the sediments and origin of the compositional variation of the BIFs

Most authors agree that BIFs are chemical sediments formed by precipitation of iron and silica from solutions consisting of a mixture of seawater with hydrothermal fluids. The main impurities are terrigenous sediments carried by rivers or winds, or deposited by volcanic

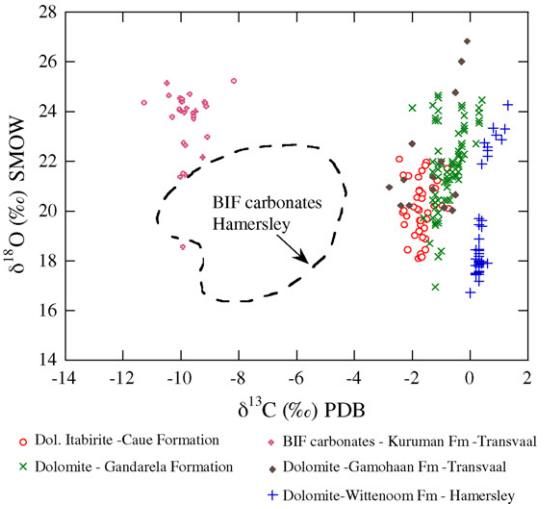

Fig. 14. Carbon and oxygen isotopes from carbonates of dolomitic itabirite of the Cauê Formation and stromatolitic dolomite of the Gandarela Formation at the Quadrilátero Ferrífero; dolomite and BIFs of the Hamersley Basin; and BIFs of the Transvaal Basin. Note the close association of dolomitic itabirite carbonates with carbonates of the Gandarela and Wittenoom Formations. The data for the Gandarela Formation are from Sial et al. (2000) and Bekker et al. (2003); that for the Hamersley Basin are from Veizer et al. (1990); and that for the Transvaal Basin from Beukes and Klein (1990).

activity (e.g., Kimberley, 1989; Klein and Beukes, 1989; Arora et al., 1995; Isley, 1995; Kato et al., 1998). Although controversies remain regarding the origin of Fe and SiO_2 in BIFs, most workers consider that these components, together with Mn and a very low amount of trace elements, are derived from the leaching of basalt and komatiites of the ocean floor by hydrothermal fluids (e.g., Dymek and Klein, 1988; Beukes and Klein, 1990; Shimizu et al., 1990; Klein and Beukes, 1992; Bau and Möller, 1993; Kato et al., 1998). Only a few authors attribute the origin of Fe and SiO_2 to the weathering of continental rocks (e.g., Holland, 1984; Manikyamba et al., 1993; Kholodov and Butuzova, 2001). This is because BIFs and deep hydrothermal deposits have the same REE signature, characterized by pronounced positive Eu anomalies and depletion of LREE (Derry and Jacobsen, 1990; Danielson et al., 1992).

BIFs of the Cauê Formation display geochemical signatures similar to those of other BIFs with very low trace element contents, high HREE fractionation, and positive Eu, Y, and La anomalies (Tables 2 and 3). The apparent negative Ce anomalies that appear in many REE patterns of itabirites are not interpreted here as true negative anomalies (which are unusual for Paleoproterozoic BIFs) because they may result from anomalous La enrichment and are not necessarily a consequence of anomalous Ce behavior. According to Bau and Dulski (1996), the combination of $(Ce/Ce^*)_{shale\ normalized} < 1$ and $(Pr/Pr^*)_{shale\ normalized} > 1$ indicates a negative Ce anomaly. Most itabirite samples show $(Ce/Ce^*)_{shale\ normalized} < 1$ and $(Pr/Pr^*)_{shale\ normalized} \cong 1$ (Appendix B). Thus, Ce_{PAAS} negative anomalies mean higher La abundances than indicated by back-extrapolation from Sm over Nd and Pr. La_{PAAS} and Y_{PAAS} anomalies are typical of recent seawater (Bau et al., 1995). In Precambrian iron formations, these anomalies are inherited from the marine surface water (Bau and Dulski, 1996). The geochemical signatures of itabirites are, therefore, consistent with the interpretation that these rocks were formed by chemical precipitation from mixtures of seawater and hydrothermal fluids. The incorporation of terrigenous sediments in BIFs of the Cauê Formation is suggested by the strong correlation between Al_2O_3 with TiO_2, Zr, and Th (Table 4). The low contents of these elements and K_2O (Table 2), however, indicate a very low degree of contamination.

In BIFs of the Hamersley and Transvaal Basins, shales and lutites are considered terrigenous deposits originated from a primary volcanogenic source (Ewers and Morris, 1981; Beukes et al., 1990; Morris, 1993). These rocks consist essentially of stilpnomelane and are chemically distinct from their host BIFs by higher contents of Al_2O_3, TiO_2, K_2O, and Zr (Horstmann and Hälbich, 1995). Itabirites of the Cauê Formation at the Águas Claras Mine do not contain interlayered shales or lutite. However, the ferrous and aluminous micaceous minerals found as thin laminas (Fig. 9D) both in the argillaceous dolomite and in the dolomite of the transition zone to the Gandarela Formation are strong evidence of the terrigenous contribution to these rocks. On the other hand, a volcanic contribution to the chemical sediments of the Cauê Formation has been recently suggested by Suckau et al. (2005) and Pires et al. (2005) but this needs to be further investigated. A better appreciation of the contribution of terrigenous components in the predominantly chemical sediments of BIFs in the QF is particularly important to understand the genesis of amphibolitic itabirite. Veríssimo (1999) and Veríssimo et al. (2002) considered the amphibolitic itabirite a silicate BIF but did not discuss its origin. We propose that silicate minerals in this itabirite type could be formed from terrigenous or volcanic components.

The mineralogy of the dolomitic and quartz itabirites, made up almost exclusively of hematite, dolomite, and quartz, provides little information about their origi-

nal composition and depositional environment of the sediments, making it difficult to understand their origin. However, major and trace element composition can provide insights on this point. Dolomitic itabirite at the Águas Claras Mine has higher average Al_2O_3 and $\sum$REE contents than quartz itabirite. This suggests a greater contribution of terrigenous material to the dolomitic itabirite and, therefore, a depositional environment closer to the continent. On the other hand, Al_2O_3 and REE contents are higher at the base of the Cauê Formation and decrease towards the top, pointing to a gradual reduction of the terrigenous flux in the Minas Basin with time.

Further constraints on the source of sediments and the paleodepositional environment of itabirites come from their $REEY_{PAAS}$ patterns. Different REE fractionation patterns of dolomitic and quartz itabirites indicate variation in the composition of seawater (Fig. 12B and E). Elderfield et al. (1990) showed that the $(Sm/Yb)_{PAAS}$ ratio and the pH are negatively correlated in seawater. The higher $(Sm/Yb)_{PAAS}$ ratio of the quartz itabirite is therefore consistent with a lower pH of the solution from which silica precipitated. $(Sm/Yb)_{PAAS}$ ratio in BIFs is controlled by marine surface water components (Bau and Möller, 1993). The differences between the REEY pattern of dolomitic and quartz itabirites shown in Fig. 12 probably reflect variation of the pH of seawater. Accordingly, dolomitic itabirite is related to more alkaline surface waters and quartz itabirite, to slightly acidic bottom water.

The precipitation of chert in the seawater is independent from the Eh conditions (Kato and Nakamura, 2003), being dependent only on the concentration of dissolved silica and on the pH of the solution. Local variations in the pH and the concentration of silica in seawater should favor the precipitation of either carbonate or chert and, together with a variable degree of terrigenous input, should control the deposition of the three major compositional types of BIFs of the Cauê Formation. The intimate association of chert and carbonate implies that their precipitation occurred under conditions close to the stability field of both minerals. Minor pH variations could be related to the upwelling of slightly acidic marine bottom waters carrying Fe hydroxides and dissolved silica onto the carbonate platform. The presence of triply layered itabirite (Fig. 6C) provides additional support for our hypothesis that pH was one of the major factors controlling the type of BIF precipitation.

The changes in the chemistry of seawater and in the input of terrigenous components could also be related to regression–transgression cycles. Changes in water depth evidenced by lithological variations in the Minas Supergroup indicate that marine transgression–regression cycles occurred during the deposition of the Minas Basin. From the Moeda Formation to the Cauê Formation, the lithological variations point to increasingly deep conditions that are associated with transgression. Additional support for marine transgression–regression cycles during the deposition of the Cauê Formation comes from the occurrence of GIF at the transition from argillaceous dolomite to ferruginous dolomite. GIF is considered to have formed by submarine reworking of earlier deposited BIFs. Regression–transgression cycles are generally responsible for such erosion, which results in deposition of eroded material close to the BIF (Simonson, 1985; Klein and Beukes, 1989; Morris, 1993). At the Águas Claras Mine GIF was formed from the erosion of older quartz itabirite. Quartz itabirite shows meso and microbanding, suggesting that it was deposited below wave-base conditions. GIF, however, has ooids and intraclasts cemented by dolomite, compatible with shallow water, above wave-base conditions. This indicates that the depositional environment was controlled by both the sea level and the seawater composition.

Deposition of BIFs during marine transgressions was suggested for BIFs of the Hamersley and Transvaal Basins (Klein and Beukes, 1989; Simonson et al., 1993; Simonson, 1996), both contemporaneous with the Minas Basin (Babinski et al., 1995b). Klein and Beukes (1989) associated the deposition of the Kuruman BIF to a major transgressive event that extensively submerged the Kaapvaal craton. Renger et al. (1994) emphasized the close similarities between the Kaapvaal and Minas Basins and suggested that the Cauê Formation in the Minas Basin is the counterpart of the Kuruman Formation in the Kaapvaal Basin. In view of the available evidence, it seems probable that BIFs of the Cauê Formation were also deposited during a major transgressive cycle in the Paleoproterozoic.

The carbon isotope signature of dolomitic itabirite is quite similar to that of stromatolitic dolomites of the Gandarela, Gamohaan, and Wittenoom Formations, but different from that of BIFs of the Transvaal and Hamersley Basins, which are more depleted in ^{13}C (Fig. 14). The Gamohaan Formation underlies the siderite BIFs of the Kuruman Formation and is composed of interbedded shale, BIFs, limestone, and dolomite. Klein and Beukes (1989) ascribe the sedimentary facies of the Gamohaan Formation to a change of only a few meters in water depth. Carbonates deposited in shallow water and BIF in deeper waters, during the peak of transgressions. Beukes et al. (1990) show that the limestone-dolomite-

shale lithologies of the Gamohaan Formation originated in a water column quite distinct from that in which the iron formations were precipitated, given that they present very distinct isotopic signature. Carbon isotope compositions of limestone-dolomite lithologies reflect the total dissolved carbon isotope composition of the whole basin water, which is similar to that of present-day oceans, i.e., close to zero. On the other hand, the depleted ^{13}C values for the siderite-rich BIFs represent a primary carbon signature of the deeper basinal waters. In view of these data we can interpret the carbon isotope signature of the dolomitic itabirite as an indication that the deposition took place in a relatively shallow water environment, shallower than that where the BIFs of the Transvaal and Hamersley Basins were deposited. Such an environment is very favorable to the facies variation observed in the Cauê Formation.

In summary, we propose that the dolomitic-, quartz-, and amphibolitic itabirites of the Cauê Formation derive from carbonate, cherty, and shaly facies of the sediments, respectively. Compositional variations of the itabirites are likely related to changes in water depth, pH, and input of terrigenous components in the sedimentation environment.

8. Conclusions

Dolomitic and quartz itabirite are metamorphosed BIFs of Paleoproterozoic age, contemporaneous to other giant BIFs of the Hamersley and Transvaal Basins. They consist of alternating millimetric to decimetric bands of predominantly dolomite and hematite, and quartz and hematite, respectively. Both rocks have a very simple chemical composition: Fe_2O_3, CaO, MgO, and LOI represent more than 98% of the average composition of dolomitic itabirite and Fe_2O_3 and SiO_2 more than 98% of the average composition of quartz itabirite. Itabirites are highly oxidized with $Fe^{3+}/(Fe^{2+} + Fe^{3+})$ ratios above 0.98, much greater than the average ratio of other Paleoproterozoic BIFs. Trace element concentrations in itabirites are very low and range from <10 ppm to between 10 and 55 ppm. Dolomitic and quartz itabirite do not differ significantly in trace element contents.

The HREE enrichment pattern exhibited by both itabirites shows a modern seawater REE signature overprinted by a hydrothermal pattern represented by positive Eu_{PAAS} anomalies. The hypothesis of a marine sedimentary origin of the dolomitic itabirite is reinforced by its REE signature and C and O isotope composition, typical of marine carbonates, and by its Y/Ho ratio very similar to that of seawater. Low Al_2O_3 and TiO_2 concentrations and a strong positive correlation between them point to a minor terrigenous component in the precipitated marine sediments of the Cauê Formation. The differences in the REE signatures of the itabirites suggest that they precipitated from aqueous solutions of different compositions. Whereas dolomitic itabirite received a more important contribution of marine surface waters, quartz itabirite formation was more influenced by marine bottom waters. Sea-level fluctuations caused by marine transgression–regressions possibly contributed to changes in the seawater composition. These changes are expressed by the co-existence of dolomitic-, quartz-, and amphibolitic itabirites, which represent lateral and vertical facies transitions of carbonatic, cherty, and shaly BIFs, respectively.

Acknowledgements

This paper is an integral part of the senior author's Ph.D. thesis presented at the Instituto de Geociências of the Universidade de São Paulo (USP). This research project was possible thanks to the grant issued by the Comissão de Aperfeiçoamento de Pessoal de Nível Superior (CAPES) to C.A.S. (grant BEX2189/02-0). C.A.S. thanks Minerações Brasileiras Reunidas (MBR) for releasing him from his usual activities as geologist during the period of his stay at the University of Queesnland. We wish to thank Eliana Maia, Jonatham Heim, and Benjamim Cohen for their thorough reviews and suggestions. A. Bekker and one anonymous reviewer are thanked for their detailed and insightful review comments.

Appendix A. Major and trace element composition

Sample	M140 Seric. Phyl.	M141 Seric. Phyl.	M132 Arg. Dol.	M134 Arg. Dol.	M135 Arg. Dol.	M137 Arg. Dol.	M138 Arg. Dol.	M139 Arg. Dol.	M4 Dol. Itabir.	M5 Dol. Itabir.	M6 Dol. Itabir.	M7 Dol. Itabir.
wt%												
SiO_2	66.38	60.28	7.37	19.19	12.48	13.01	40.27	51.57	1.97	1.27	1.73	0.80
Al_2O_3	19.69	17.52	1.81	1.72	1.23	0.61	1.42	0.05	0.77	0.33	0.72	0.26
Fe_2O_3	1.31	2.04	2.44	0.58	1.26	0.42	0.23	0.33	45.30	39.65	44.62	45.86
Fe_{tot}	1.73	5.33	8.54	4.21	5.43	5.79	3.71	2.67	46.30	40.26	45.65	46.46
FeO	0.38	2.96	5.49	3.27	3.75	4.83	3.13	2.11	0.90	0.55	0.93	0.54
MnO	<0.01	0.05	0.72	0.40	0.43	0.40	0.20	0.22	0.25	0.27	0.43	0.37
MgO	1.22	4.90	15.27	14.81	16.72	15.55	11.44	8.97	11.19	12.30	11.04	11.13
CaO	0.09	0.12	25.08	22.63	24.45	25.38	16.54	14.36	14.48	17.26	14.83	15.51
Na_2O	0.09	0.04	<0.01	<0.01	<0.01	<0.01	<0.01	<0.01	<0.01	0.05	<0.01	<0.01
K_2O	6.73	5.03	0.45	0.59	0.06	0.10	0.20	<0.01	0.11	0.06	0.05	<0.01
TiO_2	0.79	0.74	0.08	0.07	0.06	0.03	0.05	<0.01	0.04	0.01	0.06	0.01
P_2O_5	0.09	0.06	0.02	0.03	0.03	0.02	0.03	0.01	0.10	0.11	0.19	0.13
C_{tot}		0.25		10.10	11.10	11.20					6.35	
C_{grap}		0.18		0.30	0.36	0.25					<0.05	
C_{org}		0.04		0.10	0.13	0.10					0.05	
CO_2		0.11		35.50	39.00	39.70					23.10	
S	0.009	0.006	0.029	0.089	0.027	0.116	0.153	0.010	<0.001	<0.001	<0.001	<0.001
LOI	3.32	4.65	39.78	35.67	38.92	39.01	26.21	22.61	23.79	27.27	23.95	24.05
Total	100.14	98.72	99.12	99.28	99.80	99.88	100.07	100.42	99.00	99.20	98.62	96.68
ppm												
Ba	360.0	296.0	24.0	24.0	8.0	12.0	16.0	<1.0	11.0	15.0	15.0	19.0
Sr	17.0	11.0	28.0	21.0	16.0	19.0	13.0	12.0	38.0	48.0	56.0	28.0
Y	27.0	25.0	11.0	7.0	8.0	8.0	7.0	<1.0	10.0	7.0	12.0	8.0
Sc	16.0	17.0	3.0	2.0	2.0	2.0	2.0	<1.0	2.0	<1.0	2.0	<1.0
Zr	184.0	173.0	18.0	27.0	17.0	11.0	16.0	<1.0	17.0	11.0	21.0	18.0
Be	3.0	2.0	1.0	<1.0	<1.0	<1.0	<1.0	<1.0	2.0	<1.0	2.0	1.0
V	122.0	122.0	17.0	14.0	11.0	10.0	13.0	<5.0	23.5	14.3	25.8	11.9
Ni	44.5	88.4	5.3	9.4	10.2	6.6	12.3	1.4	5.6	3.5	6.9	2.8
Cu	48.3	28.0	18.9	13.0	5.7	14.5	37.5	3.9	9.5	9.4	10.7	10.9
Zn	7.6	44.0	<1.0	<1.0	<1.0	<1.0	<1.0	<1.0	9.9	13.6	16.5	3.7
Ga	27.5	23.6	2.6	2.5	1.9	1.0	2.2	<1.0	1.6	<1.0	1.4	<1.0
Ge	2.6	2.9	<0.5	<0.5	<0.5	<0.5	0.9	0.6	2.1	1.8	1.8	2.1
Rb	227.6	174.6	11.5	19.4	4.4	4.5	8.7	<1.0	5.5	<1.0	<1.0	2.2
Nb	10.6	11.6	0.9	1.0	0.8	0.4	0.9	<0.2	1.6	1.1	1.5	0.9
Mo	<2.0	<2.0	<2.0	<2.0	<2.0	<2.0	<2.0	<2.0	<2.0	<2.0	<2.0	<2.0
Ag	<0.3	<0.3	<0.3	<0.3	<0.3	<0.3	<0.3	<0.3	<0.3	<0.3	<0.3	<0.3
In	<0.1	<0.1	<0.1	<0.1	<0.1	<0.1	<0.1	<0.1	<0.1	<0.1	<0.1	<0.1
Sn	3.6	3.0	<1.0	1.1	<1.0	<1.0	<1.0	<1.0	<1.0	<1.0	<1.0	<1.0
Cs	8.7	4.9	0.4	0.8	0.3	0.1	0.3	<0.1	1.0	0.2	0.2	0.3
$\sum$REE	233.3	220.7	47.0	30.6	32.7	28.7	21.8	4.9	21.7	14.6	40.0	13.6
Hf	5.3	5.2	0.4	0.8	0.5	0.2	0.5	<0.1	0.1	0.1	0.3	<0.1
Tl	1.5	0.6	0.1	0.3	0.1	<0.1	0.2	<0.1	0.1	<0.1	0.2	0.1
Pb	22.4	7.3	<3.0	<3.0	<3.0	4.8	<3.0	<3.0	8.7	10.1	5.7	3.2
Bi	2.1	2.0	2.3	2.5	3.0	<0.1	4.0	3.0	0.4	0.1	0.2	<0.1
Th	21.7	19.1	2.6	2.4	1.5	0.7	1.3	<0.1	1.4	0.7	1.3	0.5
U	6.7	4.4	1.2	0.8	0.7	0.5	0.6	0.2	2.5	1.6	2.8	1.3
As	16.2	<5.0	5.9	6.5	<5.0	<5.0	<5.0	<5.0	9.6	5.9	15.5	<5.0
Cr	210.3	233.8	<20.0	<20.0	<20.0	<20.0	<20.0	<20.0	44.0	148.0	104.0	<20.0
Sb	4.0	1.5	0.4	0.7	0.8	0.3	0.8	<0.2	1.3	0.7	1.2	0.9
Cd	0.80	0.64	2.06	1.26	<0.30	1.24	1.67	0.75	0.73	0.84	0.55	1.15
Fe#	0.76	0.38	0.29	0.14	0.23	0.07	0.06	0.12	0.98	0.98	0.98	0.99

Sample	M8 Dol. Itabir.	M9 Dol. Itabir.	M10 Dol. Itabir.	M11 Dol. Itabir.	M96 Dol. Itabir.	P55_27 Dol. Itabir.	P55_61 Dol. Itabir.	P3_18 Quartz Itabir.	P3_23 Quartz Itabir.	P3_36 Quartz Itabir.	P3_50 Quartz Itabir.	P54_80 Quartz Itabir.
wt%												
SiO_2	0.83	0.53	0.84	0.63	1.00	0.65	0.86	61.95	49.19	39.87	30.89	19.71
Al_2O_3	0.20	0.09	0.26	0.10	0.57	0.17	0.07	0.14	0.32	0.52	0.06	0.12
Fe_2O_3	42.14	52.43	54.03	67.61	59.05	44.36	42.84	37.18	49.10	54.27	68.44	76.75
Fe_{tot}	42.92	53.00	54.92	68.11	60.03	45.02	43.33	37.37	49.37	54.51	68.66	79.34
FeO	0.70	0.51	0.80	0.45	0.88	0.59	0.44	0.17	0.24	0.22	0.20	2.33
MnO	0.28	0.23	0.27	0.18	0.25	0.32	0.25	<0.01	0.01	0.04	0.03	<0.01
MgO	12.02	9.69	9.24	6.49	7.98	11.00	11.50	0.06	0.12	0.80	0.02	0.03
CaO	16.79	13.74	12.91	9.47	11.07	15.68	16.27	0.09	0.38	1.21	0.06	0.22
Na_2O	<0.01	<0.01	<0.01	<0.01	0.27	<0.01	<0.01	<0.01	0.02	<0.01	<0.01	<0.01
K_2O	<0.01	<0.01	<0.01	0.05	<0.01	<0.01	<0.01	<0.01	<0.01	0.03	<0.01	0.01
TiO_2	0.01	0.02	0.01	0.01	0.04	0.01	<0.01	<0.01	0.01	0.03	<0.01	<0.01
P_2O_5	0.05	0.08	0.17	0.17	0.07	0.12	0.10	0.07	0.32	0.04	0.03	0.19
C_{tot}	7.05		5.50			6.90						
C_{grap}	0.05		<0.05			<0.05						
C_{org}	<0.05		0.05			<0.05						
CO_2	25.80		20.20			25.30						
S	<0.001		<0.001			0.007	0.016	0.003	0.007	<0.001	<0.001	0.003
LOI	25.97	21.33	20.10	13.49	18.33	25.68	26.49	0.21	0.46	2.23	0.40	<0.02
Total	99.03	98.71	98.72	98.70	99.55	98.60	98.92	99.85	100.21	99.27	100.08	99.61
ppm												
Ba	7.0	17.0	11.0	13.0	5.0	17.0	12.0	21.0	5.0	21.0	13.0	18.0
Sr	29.0	22.0	24.0	19.0	17.0	24.0	23.0	1.0	4.0	3.0	2.0	8.0
Y	4.0	5.0	7.0	9.0	6.0	8.0	9.0	1.0	5.0	6.0	3.0	4.0
Sc	<1.0	<1.0	<1.0	<1.0	<1.0	<1.0	<1.0	<1.0	<1.0	<1.0	<1.0	<1.0
Zr	15.0	7.0	21.0	11.0	19.0	5.0	9.0	8.0	10.0	20.0	7.0	14.0
Be	<1.0	<1.0	<1.0	<1.0	1.0	<1.0	1.0	<1.0	1.0	1.0	2.0	1.0
V	36.4	5.0	9.6	20.0	84.3	38.0	13.0	7.2	27.0	42.8	21.0	22.0
Ni	4.7	10.0	10.2	10.0	33.0	13.1	10.6	8.8	9.4	7.5	20.0	4.7
Cu	10.6	5.0	10.2	5.0	5.0	<1.0	<1.0	9.0	<1.0	11.8	<1.0	<1.0
Zn	8.4	5.0	9.3	5.0	47.5	9.4	<1.0	<1.0	2.0	<1.0	5.2	4.4
Ga	<1.0	<1.0	<1.0	<1.0	1.0	<1.0	<1.0	1.2	<1.0	1.2	<1.0	<1.0
Ge	1.9	2.1	<0.5	0.8	3.2	2.1	2.0	3.6	3.8	2.4	6.3	3.2
Rb	<1.0	<1.0	<1.0	<1.0	<1.0	<1.0	<1.0	<1.0	<1.0	1.9	<1.0	<1.0
Nb	0.8	<0.2	0.8	<0.2	1.6	0.3	0.9	0.8	0.4	0.9	0.3	0.4
Mo	<2.0	<2.0	<2.0	<2.0	<1.0	53.7	<2.0	<2.0	<2.0	<2.0	4.7	<2.0
Ag	<0.3	1.6	<0.3	1.5	<0.5	0.4	0.5	<0.3	0.4	<0.3	0.3	0.4
In	<0.1	<0.1	<0.1	<0.1	<0.1	<0.1	<0.1	<0.1	<0.1	<0.1	<0.1	<0.1
Sn	<1.0	<1.0	<1.0	4.0	<1.0	<1.0	<1.0	<1.0	<1.0	<1.0	<1.0	<1.0
Cs	<0.1	<0.1	<0.1	<0.1	<0.1	<0.1	<0.1	<0.1	<0.1	0.1	<0.1	<0.1
$\sum$REE	8.3	7.4	10.4	9.6	9.7	12.7	12.9	4.1	12.1	14.0	4.8	7.7
Hf	<0.1	0.2	<0.1	<0.1	0.2	<0.1	<0.1	0.1	<0.1	0.2	<0.1	<0.1
Tl	<0.1	<0.1	<0.1	<0.1	<0.1	<0.1	<0.1	<0.1	<0.1	<0.1	<0.1	<0.1
Pb	5.1	8.0	7.3	<3.0	<3.0	<3.0	<3.0	4.6	<3.0	<3.0	<3.0	<3.0
Bi	0.1	0.2	<0.1	0.5	0.1	5.1	6.0	0.2	4.1	<0.1	<0.1	6.5
Th	0.3	0.2	0.4	0.2	0.6	0.2	0.1	0.1	0.1	0.4	<0.1	0.1
U	1.0	1.1	1.2	2.0	4.5	2.1	2.8	1.4	2.7	3.0	1.0	1.0
As	<5.0	<5.0	<5.0	6.1	12.0	5.0	7.0	12.3	15.6	8.4	12.5	<5.0
Cr	26.0	68.0	23.0	110.0	29.0	<20.0	<20.0	<20.0	20.3	22.0	<20.0	<20.0
Sb	1.1	1.1	0.2	2.1	3.4	2.6	3.2	3.0	3.3	3.0	3.2	1.6
Cd	0.37		1.25			6.19	4.80	0.91	3.99	0.81	3.35	4.97
Fe#	0.98	0.99	0.98	0.99	0.98	0.99	0.99	0.99	0.99	1.00	1.00	0.97

Sample	P54_85 Quartz Itabir.	P54_120 Quartz Itabir.	P54_124 Quartz Itabir.	P3_69 Quartz Itabir.	P3_83 Mixed Itabir.	P3_103 Quartz Itabir.	P3_122 Mixed Itabir.	P3_138 Cherty Dol.	P3_152 Cherty Dol.	P3_170 Cherty Dol.	P3_185 Cherty Dol.	P3_196 Cherty Dol.
wt%												
SiO_2	38.18	58.82	50.43	26.62	27.74	53.28	50.34	28.21	11.08	6.56	21.06	14.58
Al_2O_3	0.10	0.13	0.13	0.09	0.44	0.12	0.08	0.73	3.07	0.27	0.55	0.33
Fe_2O_3	58.92	40.43	47.74	68.58	31.99	37.08	31.88	21.29	5.20	6.64	16.85	6.96
Fe_{tot}	60.63	40.86	49.07	68.71	33.10	37.40	32.34	22.95	9.17	8.32	18.56	11.76
FeO	1.54	0.39	1.20	0.12	1.00	0.29	0.41	1.49	3.57	1.51	1.54	4.32
MnO	<0.01	<0.01	<0.01	0.08	0.33	0.09	0.26	0.30	0.41	0.66	0.39	0.58
MgO	0.01	<0.01	0.02	0.17	8.05	1.79	3.18	10.08	18.44	17.25	12.37	13.95
CaO	0.13	0.16	0.18	1.69	11.24	2.98	5.20	13.84	21.42	25.87	17.63	22.45
Na_2O	0.02	0.02	<0.01	<0.01	0.04	0.01	0.10	0.02	0.07	0.02	<0.01	0.10
K_2O	<0.01	<0.01	0.02	0.04	0.04	<0.01	0.08	<0.01	0.10	<0.01	<0.01	<0.01
TiO_2	<0.01	<0.01	<0.01	<0.01	0.03	0.01	<0.01	0.06	0.26	0.03	0.04	0.02
P_2O_5	0.14	0.15	0.17	0.08	0.06	0.17	0.06	0.05	0.06	0.02	0.03	0.02
C_{tot}					4.80			6.05	9.65			9.80
C_{grap}					<0.05			<0.05	<0.05			<0.05
C_{org}					<0.05			<0.05	0.05			<0.05
CO_2					17.60			22.20	35.40			35.90
S	0.005	0.013	0.007	<0.001	<0.001	<0.001	<0.001	0.004	<0.001	0.038	0.014	<0.001
LOI	0.04	0.20	0.18	1.58	17.79	4.51	7.76	22.44	35.14	39.83	28.10	34.78
Total	99.25	100.34	100.17	99.05	98.86	100.33	99.40	98.62	99.21	98.81	98.71	98.56
ppm												
Ba	21.0	20.0	14.0	6.0	16.0	4.0	7.0	6.0	9.0	7.0	4.0	5.0
Sr	8.0	4.0	7.0	8.0	37.0	9.0	8.0	19.0	38.0	41.0	23.0	23.0
Y	4.0	4.0	5.0	3.0	5.0	3.0	3.0	4.0	9.0	7.0	3.0	3.0
Sc	<1.0	<1.0	<1.0	<1.0	1.0	<1.0	<1.0	2.0	4.0	<1.0	2.0	1.0
Zr	13.0	10.0	8.0	18.0	14.0	9.0	4.0	12.0	35.0	9.0	14.0	10.0
Be	1.0	<1.0	1.0	2.0	1.0	2.0	<1.0	2.0	1.0	1.0	1.0	<1.0
V	52.0	18.0	11.0	<5.0	6.5	<5.0	<5.0	10.0	32.4	6.0	9.0	<5.0
Ni	7.9	12.5	9.1	14.8	16.4	12.7	3.4	13.9	36.8	13.5	9.0	2.8
Cu	<1.0	<1.0	<1.0	9.6	5.8	<1.0	9.1	1.2	1.8	1.6	<1.0	1.9
Zn	3.6	1.9	2.8	<1.0	8.2	7.1	<1.0	18.4	20.9	<1.0	3.8	<1.0
Ga	<1.0	<1.0	<1.0	<1.0	1.2	<1.0	<1.0	1.1	5.2	<1.0	<1.0	<1.0
Ge	4.3	2.7	3.0	3.2	2.4	5.2	3.2	1.6	1.2	<0.5	0.9	<0.5
Rb	<1.0	1.7	<1.0	<1.0	1.1	<1.0	<1.0	<1.0	6.3	1.1	1.3	<1.0
Nb	0.6	2.9	0.3	0.5	1.3	<0.2	0.7	0.6	1.8	0.3	0.5	0.7
Mo	<2.0	<2.0	<2.0	<2.0	<2.0	<2.0	<2.0	<2.0	<2.0	<2.0	<2.0	<2.0
Ag	0.3	0.4	0.3	<0.3	<0.3	<0.3	<0.3	0.3	<0.3	<0.3	<0.3	<0.3
In	<0.1	<0.1	<0.1	<0.1	<0.1	<0.1	<0.1	<0.1	<0.1	<0.1	<0.1	<0.1
Sn	<1.0	<1.0	<1.0	<1.0	<1.0	<1.0	<1.0	<1.0	<1.0	<1.0	<1.0	<1.0
Cs	<0.1	0.2	0.1	<0.1	<0.1	<0.1	<0.1	<0.1	0.4	<0.1	<0.1	<0.1
$\sum$REE	5.8	9.8	8.8	7.1	7.7	7.5	4.8	10.5	15.3	10.6	9.6	7.5
Hf	<0.1	<0.1	<0.1	<0.1	0.1	<0.1	<0.1	0.2	0.5	0.2	0.2	0.1
Tl	<0.1	<0.1	<0.1	<0.1	<0.1	<0.1	<0.1	<0.1	<0.1	<0.1	<0.1	<0.1
Pb	<3.0	<3.0	<3.0	8.2	13.7	<3.0	5.6	<3.0	3.3	<3.0	<3.0	4.2
Bi	<0.1	<0.1	<0.1	<0.1	0.1	<0.1	<0.1	<0.1	0.1	<0.1	2.1	<0.1
Th	0.1	0.1	0.1	0.1	0.4	0.1	0.1	0.6	1.8	0.4	0.7	0.6
U	0.9	1.7	1.6	1.5	1.3	0.7	0.9	2.1	1.1	1.0	1.1	0.4
As	5.7	7.4	9.1	14.3	7.9	19.6	6.0	<5.0	<5.0	<5.0	<5.0	<5.0
Cr	<20.0	<20.0	<20.0	<20.0	28.0	<20.0	<20.0	164.9	<20.0	<20.0	<20.0	<20.0
Sb	2.5	2.5	3.2	2.6	2.0	2.5	1.3	0.8	0.7	0.3	0.7	0.3
Cd	5.46	2.74	3.68	0.99	0.37	2.30	0.80	2.14	0.38	2.78	2.74	0.41
Fe#	0.97	0.99	0.97	1.00	0.97	0.99	0.99	0.93	0.57	0.80	0.91	0.59

Sample	M5A	M6A	M7A	M8A	M10A	M11A	M1	M16	M81	M100	M102	M103
wt%	Iron-rich band of dolomitic itabirite							Dolomite-rich band of dolomitic itabirite				
SiO_2	1.10	1.27	0.98	0.79	0.71	0.62	0.34	0.77	0.33	0.14	2.31	0.49
Al_2O_3	0.37	0.47	0.26	0.22	0.28	0.10	0.10	0.46	0.12	0.07	1.02	0.21
Fe_2O_3	83.43	84.77	82.38	69.75	65.04	81.92	15.42	23.92	8.74	7.00	4.49	5.99
Fe_{tot}	83.74	85.13	82.61	70.11	65.57	82.23	16.06	25.00	9.48	7.21	6.15	6.55
FeO	0.28	0.32	0.21	0.32	0.48	0.28	0.58	0.97	0.67	0.19	1.49	0.50
MnO	0.07	0.06	0.11	0.18	0.20	0.10	0.48	0.55	0.62	0.54	0.32	0.48
MgO	3.00	2.92	3.36	5.76	6.51	3.09	17.35	15.99	18.86	19.73	19.72	19.34
CaO	3.59	3.08	4.28	8.03	9.18	4.56	25.12	22.62	26.82	28.40	26.40	27.80
Na_2O	<0.01	<0.01	<0.01	<0.01	<0.01	<0.01	0.02	<0.01	<0.01	0.23	0.02	0.03
K_2O	<0.01	0.06	0.02	<0.01	<0.01	<0.01	0.11	<0.01	0.01	<0.01	0.10	0.13
TiO_2	0.02	0.02	0.02	0.01	0.02	0.01	<0.01	0.03	0.02	0.01	0.05	<0.01
P_2O_5	0.12	0.04	0.04	0.11	0.18	0.20	0.22	0.06	0.02	0.04	0.02	0.02
S	<0.001	<0.001	<0.001	<0.001	0.012	0.005	<0.001	<0.001	<0.001	<0.001	<0.001	<0.001
LOI	6.83	6.07	8.13	14.17	16.30	7.93	36.88	34.51	42.63	43.91	42.39	43.55
Total	98.78	99.12	99.80	99.35	98.89	98.77	98.69	99.99	98.81	100.28	98.50	98.60
ppm												
Ba	10.0	8.0	14.0	11.0	11.0	13.0	30.0	21.0	37.0	7.0	8.0	21.0
Sr	12.0	8.0	10.0	15.0	19.0	13.0	41.0	38.0	56.0	74.0	29.0	39.0
Y	3.0	3.0	6.0	5.0	6.0	5.0	10.0	9.0	10.0	13.0	10.0	5.0
Sc	<1.0	<1.0	<1.0	<1.0	<1.0	<1.0	<1.0	<1.0	<1.0	<1.0	1.0	<1.0
Zr	15.0	15.0	15.0	14.0	14.0	15.0	7.0	15.0	9.0	1.0	10.0	6.0
Be	2.0	2.0	1.0	1.0	1.0	1.0	<1.0	1.0	<1.0	<1.0	1.0	<1.0
V	14.0	28.0	29.0	121.0	13.0	13.0	15.6	20.2	<5.0	6.9	8.8	7.5
Ni	11.2	16.7	14.5	13.4	25.2	9.8	6.4	10.9	8.4	10.0	5.5	2.6
Cu	<1.0	<1.0	<1.0	<1.0	<1.0	<1.0	7.4	4.8	2.6	11.6	1.8	2.9
Zn	13.8	13.9	14.3	11.7	11.6	12.4	9.2	4.7	10.5	5.0	4.4	<1.0
Ga	1.2	1.5	<1.0	<1.0	<1.0	<1.0	<1.0	<1.0	<1.0	<1.0	1.7	<1.0
Ge	2.6	4.0	4.5	3.1	3.2	4.2	0.6	0.7	<0.5	<0.5	<0.5	<0.5
Rb	1.6	3.8	<1.0	<1.0	<1.0	<1.0	<1.0	<1.0	<1.0	<1.0	<1.0	1.2
Nb	0.3	0.4	0.7	0.3	0.3	<0.2	1.4	0.9	0.8	0.6	1.0	0.6
Mo	<2.0	<2.0	3.9	<2.0	<2.0	<2.0	<2.0	<2.0	<2.0	<1.0	<2.0	<2.0
Ag	0.5	0.4	0.3	<0.3	0.6	0.5	<0.3	<0.3	<0.3	<0.5	<0.3	<0.3
In	<0.1	<0.1	<0.1	<0.1	<0.1	<0.1	<0.1	<0.1	<0.1	<0.1	<0.1	<0.1
Sn	<1.0	<1.0	<1.0	<1.0	1.4	<1.0	<1.0	<1.0	<1.0	<1.0	<1.0	<1.0
Cs	0.3	0.8	<0.1	<0.1	<0.1	<0.1	<0.1	<0.1	<0.1	<0.1	<0.1	<0.1
$\sum$REE	10.2	10.0	10.8	8.4	10.5	8.2	12.7	19.5	11.9	21.7	34.0	13.5
Hf	<0.1	<0.1	0.1	<0.1	<0.1	<0.1	<0.1	0.1	<0.1	<0.1	0.2	<0.1
Tl	<0.1	0.1	<0.1	<0.1	<0.1	<0.1	<0.1	<0.1	<0.1	<0.1	<0.1	0.1
Pb	<3.0	<3.0	<3.0	<3.0	<3.0	<3.0	7.0	9.4	8.2	<3.0	8.1	6.9
Bi	5.0	<0.1	<0.1	2.2	3.0	<0.1	<0.1	0.1	0.1	<0.1	0.3	<0.1
Th	0.3	0.3	0.3	0.2	0.3	0.1	2.4	0.6	0.5	0.2	1.1	0.2
U	2.9	3.0	1.5	1.7	1.4	1.9	1.3	2.3	2.1	0.9	2.4	1.1
As	<5.0	13.8	7.3	<5.0	7.6	5.6	5.8	7.1	<5.0	4.4	<5.0	6.5
Cr	81.1	<20.0	<20.0	<20.0	<20.0	<20.0	27.0	24.0	<20.0	60.0	<20.0	<20.0
Sb	0.5	1.8	1.4	1.1	1.4	1.8	0.7	0.9	1.1	0.3	1.2	4.9
Cd	2.87	4.75	6.00	4.99	4.07	5.14	0.55	0.33	0.67		0.31	0.32
Fe#	1.00	1.00	1.00	0.99	0.99	1.00	0.96	0.96	0.92	0.97	0.73	0.92

Fe_{tot} expressed as Fe_2O_3. Fe# = $Fe^{3+}/(Fe^{3+} + Fe^{2+})$.

Appendix B. Rare earth element composition (ppm)

Sample	M140	M141	M132	M134	M135	M137	M138	M139	M4	M5	M6	M7	M8	M9	M10	M11
Litho	Seric. Phyl.	Seric. Phyl.	Arg. Dol.	Arg. Dol.	Arg. Dol.	Arg. Dol.	Arg. Dol.	Arg. Dol.	Dol. Itabir.	Dol. Itabir.	Dol. Itabir.	Dol. Itabir.	Dol. Itabir.	Dol. Itabir.	Dol. Itabir.	Dol. Itabir.
La	47.32	50.86	8.93	5.18	5.93	4.92	3.38	1.01	3.89	2.46	10.92	2.29	1.52	1.08	1.71	1.43
Ce	101.83	100.90	17.57	12.29	13.08	10.40	7.66	1.86	7.17	4.92	12.88	4.21	2.42	2.21	3.00	2.75
Pr	11.68	10.33	1.95	1.52	1.46	1.32	1.00	0.22	0.82	0.56	1.44	0.49	0.32	0.28	0.39	0.38
Nd	42.65	34.19	8.08	5.70	5.70	5.45	4.21	0.91	3.64	2.49	5.97	2.25	1.48	1.25	1.90	1.69
Sm	8.32	6.15	2.23	1.16	1.32	1.17	0.96	0.19	0.81	0.55	1.16	0.51	0.29	0.33	0.40	0.44
Eu	1.87	1.44	0.96	0.46	0.43	0.45	0.31	0.07	0.34	0.24	0.56	0.25	0.14	0.11	0.17	0.18
Gd	6.32	4.59	1.88	1.09	1.07	1.20	0.93	0.18	1.06	0.73	1.59	0.71	0.45	0.45	0.62	0.60
Tb	0.90	0.75	0.34	0.19	0.20	0.22	0.18	0.03	0.20	0.14	0.28	0.13	0.08	0.08	0.11	0.11
Dy	4.75	4.33	2.04	1.03	1.27	1.26	1.04	0.16	1.32	0.90	1.91	0.92	0.54	0.51	0.73	0.69
Y	27.00	25.0	11.0	7.0	8.0	8.0	7.0	1.0	10.5	8.0	14.1	8.7	5.4	6.1	7.5	7.6
Ho	1.01	0.93	0.39	0.24	0.28	0.28	0.24	0.04	0.31	0.21	0.41	0.22	0.13	0.12	0.18	0.16
Er	3.11	2.81	1.10	0.80	0.84	0.93	0.84	0.12	0.98	0.66	1.31	0.69	0.41	0.40	0.54	0.51
Tm	0.42	0.40	0.16	0.11	0.13	0.14	0.13	0.02	0.14	0.09	0.19	0.10	0.06	0.06	0.08	0.08
Yb	2.69	2.57	1.17	0.71	0.87	0.82	0.79	0.10	0.92	0.60	1.21	0.69	0.38	0.46	0.48	0.51
Lu	0.44	0.43	0.17	0.13	0.14	0.14	0.14	0.02	0.16	0.09	0.20	0.11	0.07	0.08	0.08	0.08
$\sum$REE	260.29	245.69	57.96	37.61	40.71	36.71	28.82	5.93	32.27	22.63	54.11	22.28	13.74	13.53	17.93	17.22
La/Yb_{PAAS}	1.30	1.46	0.57	0.54	0.51	0.44	0.31	0.78	0.31	0.30	0.67	0.25	0.29	0.17	0.26	0.21
La/Nd_{PAAS}	0.98	1.32	0.98	0.81	0.92	0.80	0.71	0.98	0.95	0.88	1.62	0.90	0.92	0.77	0.80	0.75
Ce/Ce^*_{PASS}	1.00	1.02	0.97	1.01	1.03	0.94	0.96	0.90	0.93	0.97	0.75	0.91	0.80	0.92	0.85	0.86
Eu/Eu^*_{PASS}	1.21	1.27	2.21	1.95	1.69	1.79	1.57	1.84	1.73	1.79	1.95	1.97	1.88	1.42	1.62	1.61
Y/Y^*_{PASS}	0.99	0.99	0.98	1.13	1.08	1.07	1.12	1.02	1.31	1.46	1.27	1.54	1.67	2.00	1.67	1.84
Pr/Pr^*_{PASS}	1.04	1.03	0.96	1.07	0.99	1.03	1.03	1.01	0.94	0.94	0.97	0.94	0.99	1.01	0.96	1.03
La/Sm_{PAAS}	0.83	1.20	0.58	0.65	0.65	0.61	0.51	0.76	0.70	0.65	1.37	0.65	0.75	0.48	0.62	0.47
Sm/Yb_{PAAS}	1.57	1.22	0.97	0.83	0.78	0.73	0.62	1.03	0.45	0.47	0.49	0.38	0.39	0.36	0.42	0.44
Sm/Yb	3.09	2.39	1.91	1.63	1.53	1.43	1.21	2.02	0.88	0.92	0.96	0.74	0.77	0.71	0.83	0.87
Y/Ho	26.83	26.74	28.03	29.73	29.03	28.54	29.59	26.48	33.81	37.79	34.11	39.22	43.49	52.03	42.41	48.69

Sample	M96	P55_27	P55_61	P3_18	P3_23	P3_36	P3_50	P54_80	P54_85	P54_120	P54_124	P3_69	P3_83	P3_103	P3_122	P3_138
Litho	Dol. Itabir.	Dol. Itabir.	Dol. Itabir.	Quartz Itabir.	Quartz Itabir.	Quartz Itabir.	Quartz Itabir.	Quartz Itabir.	Quartz Itabir.	Quartz Itabir.	Quartz Itabir.	Qz Dol.	Qz Dol.	Qz Dol.	Qz Dol.	Qz Dol.
La	1.32	2.17	1.27	0.68	1.81	2.15	1.37	1.22	1.00	1.53	1.41	1.41	1.25	1.14	0.61	1.79
Ce	2.95	3.40	3.32	1.22	3.61	3.11	1.38	2.05	1.53	2.81	2.68	2.51	2.39	2.51	1.46	3.70
Pr	0.40	0.51	0.52	0.14	0.52	0.57	0.21	0.28	0.20	0.39	0.31	0.24	0.26	0.32	0.15	0.47
Nd	1.83	2.39	2.60	0.73	2.42	3.36	0.67	1.46	0.97	2.06	1.49	1.12	1.27	1.48	0.78	1.90
Sm	0.49	0.63	0.82	0.20	0.66	0.87	0.16	0.41	0.28	0.54	0.43	0.26	0.30	0.33	0.21	0.40
Eu	0.16	0.20	0.25	0.08	0.21	0.28	0.05	0.16	0.11	0.17	0.18	0.10	0.13	0.10	0.08	0.14
Gd	0.60	0.73	0.90	0.29	0.85	1.14	0.22	0.48	0.34	0.65	0.50	0.40	0.47	0.43	0.35	0.47
Tb	0.10	0.13	0.17	0.05	0.14	0.18	0.04	0.09	0.07	0.11	0.09	0.07	0.09	0.07	0.07	0.08
Dy	0.62	0.86	1.03	0.32	0.75	1.01	0.26	0.58	0.45	0.63	0.63	0.42	0.58	0.42	0.42	0.51
Y	6.4	8.0	9.0	2.0	5.0	7.3	3.0	4.0	4.0	4.0	5.0	3.8	5.1	3.0	3.8	4.0
Ho	0.15	0.19	0.23	0.06	0.17	0.20	0.06	0.13	0.10	0.13	0.13	0.09	0.13	0.10	0.09	0.12
Er	0.47	0.63	0.71	0.18	0.46	0.56	0.17	0.38	0.32	0.40	0.41	0.26	0.40	0.30	0.26	0.39

Sample	M96	P55_27	P55_61	P3_18	P3_23	P3_36	P3_50	P54_80	P54_85	P54_120	P54_124	P3_69	P3_83	P3_103	P3_122	P3_138
Litho	Dol. Itabir.	Dol. Itabir.	Dol. Itabir.	Quartz Itabir.	Quartz Itabir.	Quartz Itabir.	Quartz Itabir.	Quartz Itabir.	Quartz Itabir.	Quartz Itabir.	Quartz Itabir.	Qz Dol.	Qz Dol.	Qz Dol.	Qz Dol.	Qz Dol.
Tm	0.07	0.10	0.12	0.03	0.06	0.08	0.03	0.06	0.05	0.06	0.06	0.04	0.06	0.04	0.03	0.06
Yb	0.49	0.66	0.79	0.14	0.33	0.44	0.17	0.35	0.32	0.32	0.40	0.21	0.36	0.27	0.21	0.36
Lu	0.08	0.10	0.13	0.02	0.05	0.07	0.02	0.05	0.05	0.05	0.06	0.04	0.06	0.04	0.04	0.06
$\sum$REE	16.11	20.71	21.87	6.13	17.05	21.27	7.80	11.70	9.78	13.85	13.81	10.91	12.81	10.54	8.56	14.47
La/Yb_{PAAS}	0.20	0.24	0.12	0.35	0.40	0.36	0.60	0.26	0.23	0.35	0.26	0.50	0.26	0.31	0.22	0.36
La/Nd_{PAAS}	0.64	0.81	0.43	0.83	0.66	0.57	1.83	0.74	0.92	0.66	0.84	1.12	0.87	0.69	0.70	0.84
Ce/Ce^*_{PASS}	0.94	0.74	0.94	0.92	0.86	0.65	0.60	0.81	0.79	0.84	0.93	1.00	0.96	0.96	1.09	0.93
Eu/Eu^*_{PASS}	1.40	1.37	1.38	1.50	1.33	1.33	1.18	1.72	1.67	1.36	1.80	1.42	1.58	1.30	1.43	1.49
Y/Y^*_{PASS}	1.70	1.58	1.49	1.13	1.11	1.30	1.94	1.18	1.51	1.13	1.37	1.56	1.50	1.19	1.53	1.29
Pr/Pr^*_{PASS}	1.01	1.06	1.04	0.87	1.04	1.03	1.27	0.94	0.96	0.96	0.92	0.83	0.89	0.97	0.85	1.04
La/Sm_{PAAS}	0.39	0.50	0.22	0.50	0.40	0.36	1.26	0.43	0.53	0.41	0.48	0.79	0.60	0.50	0.42	0.65
Sm/Yb_{PAAS}	0.51	0.48	0.52	0.70	1.01	0.99	0.48	0.60	0.44	0.85	0.54	0.63	0.43	0.62	0.52	0.56
Sm/Yb	1.00	0.95	1.03	1.37	1.98	1.96	0.94	1.18	0.87	1.68	1.07	1.25	0.85	1.23	1.03	1.10
Y/Ho	43.80	41.74	39.88	32.04	29.25	36.82	51.30	31.62	40.14	31.47	37.23	42.33	40.28	31.00	40.46	32.99

Sample	P3_152	P3_170	P3_185	P3_196	M5A	M6A	M7A	M8A	M10A	M11A	M1	M16	M81	M100	M102	M103
Litho	Qz Dol.	Qz Dol.	Qz Dol.	Qz Dol.	Hem. Bd	Hem. Bd	Hem. Bd	Hem. Bd	Hem. Bd	Hem. Bd	Dol. Bd	Dol. Bd	Dol. Bd	Dol. Bd	Dol. Bd	Dol. Bd
La	1.63	1.37	1.65	1.26	1.90	1.88	2.56	1.61	1.89	1.28	1.88	2.87	2.37	3.60	5.67	2.40
Ce	4.64	3.24	3.46	2.74	3.42	3.41	3.49	2.44	2.94	2.30	3.34	6.41	3.10	6.85	13.02	4.70
Pr	0.52	0.41	0.42	0.29	0.41	0.39	0.43	0.33	0.41	0.33	0.52	0.86	0.46	0.84	1.31	0.55
Nd	2.65	1.84	1.82	1.26	1.77	1.60	1.66	1.58	2.02	1.50	2.52	4.04	2.06	3.55	5.83	2.48
Sm	0.78	0.55	0.38	0.29	0.41	0.39	0.37	0.32	0.48	0.38	0.60	0.91	0.45	0.79	1.33	0.53
Eu	0.21	0.17	0.10	0.10	0.15	0.15	0.14	0.13	0.14	0.15	0.24	0.31	0.18	0.39	0.57	0.25
Gd	1.04	0.76	0.41	0.37	0.49	0.42	0.38	0.44	0.57	0.55	0.90	1.14	0.64	1.06	1.51	0.67
Tb	0.21	0.15	0.08	0.07	0.08	0.07	0.07	0.08	0.10	0.09	0.14	0.18	0.12	0.20	0.27	0.11
Dy	1.35	0.81	0.43	0.43	0.51	0.53	0.55	0.46	0.66	0.57	0.92	1.12	0.81	1.36	1.73	0.71
Y	8.8	7.0	3.0	3.4	3.0	3.0	6.0	5.0	6.0	5.0	10.5	9.3	9.5	13.5	10.7	5.3
Ho	0.29	0.18	0.10	0.10	0.13	0.12	0.12	0.11	0.15	0.14	0.21	0.23	0.20	0.33	0.38	0.16
Er	0.87	0.56	0.32	0.28	0.41	0.40	0.41	0.38	0.50	0.45	0.67	0.65	0.65	1.15	1.12	0.43
Tm	0.13	0.08	0.05	0.04	0.06	0.06	0.07	0.06	0.08	0.06	0.09	0.09	0.10	0.19	0.15	0.06
Yb	0.86	0.45	0.31	0.25	0.40	0.41	0.48	0.38	0.50	0.38	0.56	0.57	0.60	1.20	0.99	0.36
Lu	0.15	0.07	0.05	0.04	0.07	0.07	0.08	0.06	0.08	0.06	0.10	0.10	0.11	0.19	0.17	0.06
$\sum$REE	24.10	17.65	12.57	10.91	13.21	12.91	16.83	13.38	16.53	13.24	23.19	28.80	21.35	35.18	44.77	18.76
La/Yb_{PAAS}	0.14	0.22	0.40	0.38	0.35	0.34	0.39	0.32	0.28	0.25	0.25	0.37	0.29	0.22	0.42	0.49
La/Nd_{PAAS}	0.55	0.66	0.81	0.89	0.96	1.04	1.37	0.91	0.83	0.75	0.66	0.63	1.02	0.90	0.86	0.86
Ce/Ce^*_{PASS}	1.16	1.00	0.96	1.05	0.89	0.91	0.76	0.77	0.77	0.82	0.78	0.94	0.68	0.91	1.10	0.94
Eu/Eu^*_{PASS}	1.09	1.26	1.24	1.35	1.60	1.70	1.70	1.59	1.30	1.53	1.54	1.42	1.60	1.98	1.90	2.01
Y/Y^*_{PASS}	1.13	1.48	1.16	1.31	0.94	0.94	1.84	1.74	1.50	1.41	1.89	1.48	1.86	1.60	1.06	1.24
Pr/Pr^*_{PASS}	0.88	0.99	0.99	0.91	0.99	0.99	1.06	0.99	0.99	1.03	1.06	0.99	1.08	1.01	0.89	0.95
La/Sm_{PAAS}	0.30	0.36	0.63	0.62	0.67	0.70	0.99	0.72	0.57	0.49	0.45	0.46	0.76	0.66	0.62	0.66
Sm/Yb_{PAAS}	0.46	0.62	0.63	0.61	0.52	0.49	0.39	0.44	0.49	0.51	0.54	0.81	0.38	0.34	0.68	0.74
Sm/Yb	0.91	1.22	1.24	1.20	1.03	0.96	0.77	0.86	0.96	1.01	1.07	1.60	0.75	0.66	1.34	1.46
Y/Ho	30.78	39.73	30.66	34.07	23.98	24.66	48.27	44.36	38.88	36.07	49.50	41.16	46.63	40.85	28.39	32.83

Y content is not included in $\sum$REE. $(Eu/Eu^*)_{PAAS} = ((Eu/Eu_{PAAS})/(Sm/Sm_{PAAS}) \times (Gd/Gd_{PAAS}))^{1/2}$, Ce/Ce^*_{PASS} and Y/Y^*_{PASS} calculated by similar way. Hem. Bd = iron-rich band of dolomitic itabirite; Dol. Bd = dolomite-rich band of dolomitic itabirite.

References

Alkmim, F.F., Marshak, S., 1998. Transamazonian orogeny in the São Francisco craton, Minas Gerais, Brazil: evidence for Paleoproterozoic collision and collapse in the Quadrilátero Ferrífero. Precambrian Res. 90, 29–58.

Arora, M., Govil, P.K., Charan, S.N., Uday Raj, B., Balaram, V., Manikyamba, C., Chatterjee, A.K., Naqvi, S.M., 1995. Geochemistry and origin of Archean banded iron-formation from the Bababudan Schist Belt, India. Econ. Geol. 90, 2040–2057.

Babinski, M., Chemale Jr., F., Van Schmus, W.R., 1995a. The Pb/Pb ages of the Minas Supergroup carbonate rocks, Quadrilátero Ferrífero, Brazil. Precambrian Res. 72, 235–245.

Babinski, M., Chemale Jr., F., Van Schmus, W.R., 1995b. Cronoestratigrafia do Supergrupo Minas e provável correlação de suas formações ferríferas com similares da África do Sul e Austrália. Geochim. Brasiliensis 9 (1), 33–46.

Bau, M., Möller, P., 1993. Rare earth element systematics of the chemically precipitated component in early Precambrian iron formations and the evolution of the terrestrial atmosphere–hydrosphere–lithosphere system. Geochim. Cosmochim. Acta 57, 2239–2249.

Bau, M., Dulski, P., 1996. Distribution of yttrium and rare-earth elements in the Penge and Kuruman iron-formations, Transvaal Supergroup, South Africa. Precambrian Res. 79, 37–55.

Bau, M., Dulski, P., Möller, P., 1995. Yttrium and holmium in South Pacific seawater: vertical distribution and possible fractionation mechanisms. Chem. Erde. 55, 1–15.

Bekker, A., Sial, A.N., Karhu, J.A., Ferreira, V.P., Noce, C.M., Kaufman, A.J., Romano, A.W., Pimentel, M.M., 2003. Chemostratigraphy of carbonates from the Minas Supergroup, Quadrilátero Ferrífero (Iron Quadrangle), Brazil: a stratrigraphic record of early Proterozoic atmospheric, biogeochemical and climatic change. Am. J. Sci. 303, 865–904.

Beukes, N.J., 1980. Lithofacies and stratigraphy of the Kuruman and Griquatown iron-formations, northern Cape Province, South Africa. Trans. Geol. Soc. SA 83, 69–86.

Beukes, N.J., 1984. Sedimentology of the Kuruman and Griquatown Iron-formations, Transvaal Supergroup, Griqualand West, South Africa. Precambrian Res. 24, 47–84.

Beukes, N.J., Klein, C., 1990. Geochemistry and sedimentology of a facies transition – from microbanded to granular iron-formation – in the early Proterozoic Transvaal Supergroup, South Africa. Precambrian Res. 47, 99–139.

Beukes, N.J., Gutzmer, J., Mukhopadhyay, J., 2002. The geology and genesis of high-grade iron ore deposits, Iron Ore 2002. Australasian Institute of Mining and Metallurgy, Perth, pp. 23–29.

Beukes, N.J., Klein, C., Kaufman, A.J., Hayes, J.M., 1990. Carbonate petrography, kerogen distribution, and carbon and oxygen isotope variations in an early Proterozoic transition from limestone to iron-formation deposition, Transvaal Supergroup, South Africa. Econ. Geol. 85 (4), 663–690.

Chemale Jr., F., Rosière, C.A., Endo, I., 1994. The tectonic evolution of the Quadrilátero Ferrífero, Minas Gerais, Brazil. Precambrian Res. 65, 25–54.

Cordani, U.G., Kawashita, K., Müller, G., Quade, H., Reimer, V., Roeser, H., 1980. Interpretação tectônica e petrológica de dados geocronológicos do embasamento na borda sudeste do Quadrilátero Ferrífero. Anais da Academia Brasileira de Ciências 52, 785–799.

Dalstra, H.J., Guedes, S., 2004. Giant hydrothermal hematite deposits with Mg-Fe metasomatism: a comparison of the Carajás, Hamersley, and other iron mines. Econ. Geol. 99, 1793–1800.

Danielson, A., Möller, P., Dulski, P., 1992. The europium anomalies in banded iron formations and the thermal history of the oceanic crust. Chem. Geol. 97, 89–100.

Davis, B., Hippert, J., 2000. Dome emplacement and formation of kilometre-scale synclines in a granite-greenstone terrain (Quadrilátero Ferrífero, southeastern Brazil). Precambrian Res. 102, 99–121.

Derry, L.A., Jacobsen, S.B., 1990. The chemical evolution of Precambrian seawater: evidence from REEs in banded iron formations. Geochim. Cosmochim. Acta 54, 2965–2977.

Dorr, J.V.N., 1969. Physiographic, stratigraphic and structural development of the Quadrilátero Ferrífero, Minas Gerais, Brazil. U.S.G.S. Prof. Paper, 614-A, Washington, DC, 110 pp.

Dorr, J.V.N., 1973. Iron-formation in South America. Econ. Geol. 68, 1005–1022.

Dymek, R.F., Klein, C., 1988. Chemistry, petrology and origin of banded iron-formation lithologies from the 3800 Ma Isua supracrustal belt West Greenland. Precambrian Res. 39, 247–302.

Elderfield, H., Upstill-Goddard, R., Sholkovitz, E.R., 1990. The rare earth elements in rivers, estuaries, and coastal seas and their significance to the composition of ocean waters. Geochim. Cosmochim. Acta 54, 971–991.

Ewers, W.E., Morris, R.C., 1981. Studies of the Dales Gorge Member of the Brockman Iron Formation Western Australia. Econ. Geol. 76, 1929–1953.

Floran, R.J., Papike, J.J., 1978. Mineralogy and petrology of the Gunflint Iron Formation Minnesota-Ontario: correlation of compositional and assemblage variations at low to moderate grade. J. Petrol. 19 (2), 215–288.

Gnaneshwar Rao, T., Naqvi, S.M., 1995. Geochemistry, depositional environment and tectonic setting of the BIF's of the late Archean Chitradurga Schist Belt, India. Chem. Geol. 121, 217–243.

Goode, A.D.T., Hall, W.D.M., Bunting, J.A., 1983. The Nabberu basin of Western Australia. In: Trendall, A.F., Morris, R.C. (Eds.), Iron-Formation Facts and Problems. Developments in Precambrian Geology 6. Elsevier, New York, pp. 295–323.

Gromet, L.P., Dymek, R.F., Haskin, L.A., Korotev, R.L., 1984. The "North American shale composite": its compilation, major and trace element characteristics. Geochim. Cosmochim. Acta 48, 2469–2482.

Gross, G.A., 1980. A classification of iron formations based on depositional environments. Can. Mineral. 18, 215–222.

Hall, W.D.M., Goode, A.D.T., 1978. The early Proterozoic Nabberu basin and associated iron formations of Western Australia. Precambrian Res. 7, 129–184.

Herz, N., 1978. Metamorfic rocks of the Quadrilátero Ferriífero, Minas Gerais, Brazil, 641-C. USGS Prof. Paper.

Holland, H.D., 1984. The Chemical Evolution of the Atmosphere and the Oceans. Princeton University Press, Princeton, 582 pp.

Horstmann, U.E., Hälbich, I.W., 1995. Chemical composition of banded iron-formations of the Griqualand West Sequence, Northern Cape Province, South Africa, in comparison with other Precambrian iron formations. Precambrian Res. 72, 109–145.

Isley, A.E., 1995. Hydrothermal plumes and the delivery of iron to banded iron formation. J. Geol. 103, 169–185.

James, H.L., 1954. Sedimentary facies of iron-formations. Econ. Geol. 49, 235–293.

Kato, Y., Nakamura, K., 2003. Origin and global tectonic significance of Early Archean cherts from the Marble Bar greenstone

belt, Pilbara craton Western Australia. Precambrian Res. 125, 191–243.

Kato, Y., Ohta, I., Tsunematsu, T., Watanabe, Y., Isozaki, Y., Maruyama, S., Imai, N., 1998. Rare earth element variations in mid-Archean banded iron formations: implications for the chemistry of ocean and plate tectonics. Geochim. Cosmochim. Acta 62 (21/22), 3475–3497.

Kholodov, V.N., Butuzova, G.Y., 2001. Problems of iron and phosphorus geochemistry in the Precambrian. Lithol. Miner. Resour. 36 (4), 291–302.

Kimberley, M.M., 1989. Exhalative origins of iron formations. Ore Geol. Rev. 5, 13–145.

Klein, C., Fink, R.P., 1976. Petrology of the Sokoman Iron Formation in the Howells River Area, at the Western Edge of the Labrador Trough. Econ. Geol. 71, 453–487.

Klein, C., Beukes, N.J., 1989. Geochemistry and sedimentology of a facies transition from limestone to iron-formation deposition in the Early Proterozoic Transvaal Supergroup, South Africa. Econ. Geol. 84 (7), 1733–1774.

Klein, C., Beukes, N.J., 1992. Time distribution, stratigraphy, sedimentologic setting, and geochemistry of Precambrian iron-formations. In: Schopf, J.W., Klein, C. (Eds.), The Proterozoic Biosphere. Cambridge University Press, Cambridge, pp. 139–146.

Klein, C., Ladeira, E.A., 2000. Geochemistry and petrology of some Proterozoic banded iron-formations of the Quadrilátero Ferrífero, Minas Gerais, Brazil. Econ. Geol. 95, 405–428.

Lindenmayer, Z.G., Laux, J.H., Teixeira, J.B.G., 2001. Considerações sobre a origem das formações ferríferas da Formação Carajás, Serra dos Carajás. Revista Brasileira de Geociências 31 (1), 21–28.

Macambira, J.B., Schrank, A., 2002. Químio-estratigrafia e evolução dos jaspilitos da Formação Carajás (PA). Revista Brasileira de Geociências 32 (4), 567–578.

Manikyamba, C., 1988. Petrology and geochemistry of mixed oxide-silicate facies banded iron formations from Sandur Schist Belt, India. J. Geol. Soc. Ind. 52, 651–661.

Manikyamba, C., Balaram, V., Naqvi, S.M., 1993. Geochemical signatures of polygenetic origin of a banded-iron formation (BIF) of the Archean Sandur greenstone belt (schist belt) Karnataka nucleus, India. Precambrian Res. 61, 137–164.

Marshak, S., Alkmim, F.F., 1989. Proterozoic contraction/extension tectonics of the southern São Francisco craton region, Minas Gerais, Brazil. Tectonics 8 (3), 551–571.

McLennan, S.B., 1989. Rare earth elements in sedimentary rocks Influence of provenance and sedimentary processes. In: Lipin, B.R., McKay, G.A. (Eds.), Geochemistry and Mineralogy of the Rare Earth Elements. Miner. Soc. Am., Washington, pp. 169–200.

Morris, R.C., 1993. Genetic modeling for banded iron formation of the Hamersley Group, Pilbara Craton Western Australia. Precambrian Res. 60, 243–286.

Nozaki, Y., Zhang, J., Amakawa, H., 1997. The fractionation between Y and Ho in the marine environment. Earth Planet. Sci. Lett. 148, 329–340.

Pomerene, J.B., 1964. Geology and mineral deposits of the Belo Horizonte, Ibirité and Macacos quadrangles. USGS Prof. Paper 341-D, pp. 1–84.

Pires, F.R.M., 1979. Structural geology and stratigraphy at the junction of the Serra do Curral anticline and the Moeda syncline, Quadrilátero Ferrífero, Minas Gerais, Brazil. Ph.D. Thesis, Michigan Tech. University, Ann Arbor, 220 pp.

Pires, F.R.M., 1995. Textural and mineralogical variations during metamorphism of the Proterozoic Itabira Iron Formation in the Quadrilátero Ferrífero, Minas Gerais, Brazil. Anais da Academia Brasileira de Ciências 67 (1), 77–105.

Pires, F.R.M., Aranha, D.M., Cabral, A.R., 2005. Volcanic origin of the Proterozoic Itabira Iron Formation, Quadrilátero Ferrífero, Minas Gerais, Brazil, Iron Ore 2005, Abstracts, Fremantle.

Renger, F.E., Noce, C.M., Romano, A.W., Machado, N., 1994. Evolução sedimentar do Supergrupo Minas: 500 Ma de registro geológico no Quadrilátero Ferrífero, Minas Gerais, Brasil. Geonomos 2 (1), 1–11.

Rosière, C.A., 1981. Strukturelle und texturelle untersuchungen in der eisenerzlagerstaette "Pico de Itabira" bei itabirito, Minas Gerais, Brasilien. Ph.D. Thesis. Clausthaler Geowissenschaftliche Dissertationen 9, Clausthal Zellerfeld, p. 302.

Rosière, C.A., Chemale Jr., F., Guimarães, M.L.V., 1993. Um modelo para a evolução microestrutural dos minérios de ferro do Quadrilátero Ferrífero: Parte I—estruturas e recristalização. Geonomos 1 (1), 65–84.

Rosière, C.A., Siemes, H., Quade, H., Brokmeier, H., Jansen, E.M., 2001. Microstructures, textures and deformation mechanisms in hematite. J. Struct. Geol. 23, 1429–1440.

Shimizu, H., Umemotto, N., Masuda, A., Appel, P.W.U., 1990. Sources of iron-formations in the Archean Isua and Malene supracrustals West Greenland: evidence from La-Ce and Sm-Nd isotopic data and REE abundances. Geochim. Cosmochim. Acta 54, 1147–1154.

Sial, A.N., Ferreira, V.P., Almeida, A.R., Romano, A.W., Parente, C.V., Costa, M.L., Santos, V.H., 2000. Carbon isotope fluctuations in Precambrian carbonate sequences of several localities in Brazil. Anais da Academia Brasileira de Ciências 72 (4), 539–558.

Simonson, B.M., 1985. Sedimentological constraints on the origin of Precambrian iron-formations. Geol. Soc. Am. Bull. 104, 244–252.

Simonson, B.M., 1996. Was the deposition of large Precambrian iron formations linked to major marine transgressions? J. Geol. 104, 665–676.

Simonson, B.M., Schubel, K.A., Hassler, S.W., 1993. Carbonate sedimentology of the early Precambrian Hamersley Group of Western Australia. Precambrian Res. 60, 287–335.

Souza, P.C., Müller, G., 1984. Primeiras estruturas algais comprovadas na Formação Gandarela Quadrilátero Ferrífero. Revista Escola de Minas de Ouro Preto 2, 13–21.

Spier, C.A., 2005. Geoquímica e gênese das formações ferríferas bandadas e do minério de ferro da Mina de Águas Claras, Quadrilátero Ferrífero, MG. Ph.D. Thesis, Universidade de São Paulo, São Paulo, 298 pp.

Spier, C.A., Oliveira, S.M.B., Rosière, C.A., 2003. Geology and geochemistry of the Águas Claras and Pico iron mines, Quadrilátero Ferrífero, Minas Gerais, Brazil. Mineralium Deposita 38, 751–774.

Spier, C.A., Vasconcelos, P.M., Oliveira, S.M.B., 2006. $^{40}Ar/^{39}Ar$ geochronological constraints on the evolution of lateritic iron deposits in the Quadrilátero Ferrífero, Minas Gerais, Brazil. Chem. Geol. 234, 79–104.

Suckau, V.E., Suita, M.T.F., Zapparolli, A.C., Spier, C.A., Ribeiro, D.T., 2005. Transitional pyroclastic, volcanic-exhalative rocks to iron ores in the Cauê Formation, Tamanduá and Capitão do Mato Mines: an overview of metallogenetic and tectonic aspects, III Simpósio do Cráton de São Francisco, Anais, CBPM/UFBA/SBG, Salvador, pp. 343–346.

Taylor, D., Dalstra, H.J., Harding, A.E., Broadbent, G.C., Barley, M.E., 2001. Genesis of the high-grade hematite orebodies of the Hamerley Province Western Australia. Econ. Geol. 96, 837–873.

Teixeira, W., Figueiredo, M.C.H., 1991. An outline of Early Proterozoic crustal evolution in the São Francisco craton, Brazil: a review. Precambrian Res. 53, 1–22.

TEX Report, 2005. Iron Ore Manual 2003–2004. The TEX Report, Tokyo, 365 pp.

Thorne, W.S., Hagemann, S.G., Barley, M.E., 2004. Petrographic and geochemical evidence for hydrothermal evolution of the North Deposit, Mt Tom Price Western Australia. Mineralium Deposita 39 (7), 766–783.

Trendall, A.F., 2002. The significance of iron-formation in the Precambrian stratigraphic record. In: Altermann, W., Corcoran, P.L. (Eds.), Precambrian Sedimentary Environments: A Modern Approach to Ancient Depositional Systems. Special Publication Number 53 of the International Association of Sedimentologists. Blackwell Science.

Trendall, A.F., Blockley, J.G., 1970. The iron formations of the Precambrian Hamersley Group, Western Australia, with special reference to the associated crocidolite. WA Geol. Surv. Bull. 119, 365.

Veizer, J., Clayton, R.N., Hinton, R.W., 1992. Geochemistry of Precambrian carbonates: IV. Early Paleoproterozoic (2.25 ± 0.25 Ga) seawater. Geochim. Cosmochim. Acta 56, 2487–2501.

Veizer, J., Hoefs, J., Lowe, D.R., Thurston, P.C., 1989. Geochemistry of Precambrian carbonates: II. Archean greenstone belts and Archean sea water. Geochim. Cosmochim. Acta 53, 859–871.

Veizer, J., Clayton, R.N., Hinton, R.W., Von Burn, V., Mason, T.R., Buck, S.G., Hoefs, J., 1990. Geochemistry of Precambrian carbonates: 3-shelf seas and non-marine environments of the Archean. Geochim. Cosmochim. Acta 54, 2717–2729.

Veríssimo, C., 1999. Jazida de Alegria: Gênese e tipologia dos minérios de ferro (Minas 3, 4 e 5—Porção Ocidental). Ph.D. Thesis, Universidade Estadual Paulista—UNESP, Rio Claro, 234 pp.

Veríssimo, C.U.V., Schrank, A., Pires, F.R.M., Hasui, Y., Zanardo, A., Parente, C.V., 2002. Geochemical study of the itabirite iron ores of the Alegria mine—Quadrilátero Ferrífero, Minas Gerais, Brazil, Iron Ore 2002. Australasian Institute of Mining and Metallurgy, Perth, pp. 95–103.

Viel, R.S., Moreira, P.C.H., Alkmim, F.F., 1987. Faciologia da Formação Cauê e gênese do minério de ferro friável da Mina de Águas Claras, Serra do Curral-Minas Gerais, Simpósio sobre sistemas deposicionais no Pré-Cambriano. Sociedade Brasileira de Geologia—Núcleo MG Ouro Preto, 137–153.

Villaça, J.N., 1981. Alguns aspectos sedimentares da Formação Moeda. Boletim da Sociedade Brasileira de Geologia de Minas Gerais 2, 93–137.

Wallace, R.M., 1965. Geology and mineral resources of the Pico do Itabirito District, Minas Gerais, Brazil. U.S. Geol. Survey Prof. Paper 341-F, 68 pp.

Warren, J., 2000. Dolomite: occurrence, evolution and economically important associations. Earth Sci. Rev. 52, 1–81.